DESIGN, FABRICATION AND CHARACTERIZATION OF SURFACE PLASMON RESONANCE BASED MEMS DISPLACEMENT SENSORS

A THESIS
SUBMITTED TO THE GRADUATE PROGRAM OF MATERIALS SCIENCE AND NANOTECHNOLOGY
AND THE INSTITUTE OF ENGINEERING AND SCIENCES
OF BILKENT UNIVERSITY
IN PARTIAL FULLFILMENT OF THE REQUIREMENTS
FOR THE DEGREE OF
MASTER OF SCIENCE

By
Hasan Güner
August, 2009

I certify that I have read this thesis and that in my opinion it is fully adequate, in scope and in quality, as a thesis for the degree of Master of Science.

Prof. Dr. Salim Çıracı (Supervisor)

I certify that I have read this thesis and that in my opinion it is fully adequate, in scope and in quality, as a thesis for the degree of Master of Science.

Res. Assist. Prof. Dr. Aykutlu Dâna (Co-supervisor)

I certify that I have read this thesis and that in my opinion it is fully adequate, in scope and in quality, as a thesis for the degree of Master of Science.

Assist. Prof. Dr. Mehmet Bayındır

I certify that I have read this thesis and that in my opinion it is fully adequate, in scope and in quality, as a thesis for the degree of Master of Science.

Assist. Prof. Dr. Ali Kemal Okyay

Approved for the Institute of Engineering and Sciences:

Prof. Dr. Mehmet B. Baray
Director of Institute of Engineering and Sciences

ABSTRACT

DESIGN, FABRICATION AND CHARACTERIZATION OF SURFACE PLASMON RESONANCE BASED MEMS DISPLACEMENT SENSORS

Hasan Güner

M. Sc., Department of Materials Science and Nanotechnology

Supervisor: Prof. Dr. Salim Çıracı

August, 2009

Strong dependence of surface plasmon resonance (SPR) on coupling parameters offers new varieties of sensing mechanisms in nano and micro-scale engineering fields. In this study, design, fabrication and characterization of MEMS displacement sensors that utilize angular dependence of grating coupled SPR condition are explored.

Several surface plasmon polariton (SPP) excitation mechanisms are reported in the academic literature. One of them which is quite adaptable to microelectromechanical systems is grating coupling scheme. In this scheme, thin metallized grating structures are particularly designed depending on the desired wavelength and the angle of incidence of the SPP excitation light. Geometric parameters like periodicity, surface profile, depth and duty cycle of the grooves and material parameters like dispersion and thickness of the top metal layer have to be chosen with care in order to reach sharp SPR curves in the reflected intensity spectra with respect to either wavelength or angle of incidence. As the first step, geometric and material parameters of SPR gratings are numerically optimized using rigorous coupled-wave analysis (RCWA). Angular quality factors on the order of tens are shown to be achievable. Various lithographic techniques (nanoimprint, electron beam and optical lithography) are used to nanofabricate those certainly defined gratings. It is observed that p-polarized reflected intensity measurements using spectroscopic ellipsometry are in quite good agreement with those numerically calculated. Spectroscopic scan measurements are also provided to show the polarization dependence of SPP excitation.

All effort to obtain high angular Q-factor grating structures is aimed at enhancing the sensitivity of angular displacement detection scheme. In this scheme, angular position of the grating structure in the polarization plane is detected through the reflected intensity response of the photodetector. Dependence of sensitivity on excitation light source wavefront parameters and photodetector noise are analyzed.

MEMS displacement sensor designs relying on the principle of angular displacement detection scheme are developed. Simply, SPR grating structures are transferred on conventional micromembranes. Two types of such particular designed micromembranes are introduced: corrugated microcantilevers (singly clamped) and corrugated microbridges (doubly clamped). They are fabricated through well-known surface micromachining processes in addition to SPR grating nanofabrication procedures. Mechanical resonance frequencies, flexural mode shapes and effective spring constants are analytically, numerically and experimentally obtained. In addition, a MEMS accelerometer design with plasmonic readout with nano-G noise floor is presented. An experimental configuration for micromechanical displacement sensing is investigated. According to the results of this work, novel arrayed sensors combining the sensitivities of plasmon resonance and micromembrane type sensors may provide unprecedented performance.

Keywords: Plasmonics, Grating Coupled Surface Plasmon Resonance, MEMS Sensors, Micromechanical Displacement Detection

ÖZET

YÜZEY PLAZMON REZONANSINA DAYALI MEMS YERDEĞİŞTİRME ALGILAYICILARININ TASARIM, ÜRETİM VE KARAKTERİZASYONU

Hasan Güner

Tez Yöneticisi: Prof. Dr. Salim Çıracı

Yüksek Lisans, Malzeme Bilimi ve Nanoteknoloji Bölümü

Ağustos, 2009

Yüzey plazmon rezonansının kuplaj parametrelerine sıkı bağımlılığı nano ve mikro-ölçekli mühendislik sahalarında yeni tür algılama mekanizmalarına olanak sağlamaktadır. Bu çalışmada, kırınım ağı kuplajlı yüzey plazmon rezonans şartının açı bağımlılığından faydalanan MEMS yerdeğiştirme algılayıcılarının tasarım, üretim ve karakterizasyonu açıklandı.

Yüzey plazmon polariton uyarımına dair çeşitli mekanizmalar akademik literatürde anlatılagelmektedir. Bu mekanizmalardan mikroelektromekanik sistemlere oldukça uyarlanabilir olanlarından biri kırınım ağıyla kuplaj şemasıdır. Bu şemada, ince metal kaplı kırınım ağı yapıları, istenen yüzey plazmon polaritonu uyarım ışığı dalgaboyu ve geliş açısına bağlı olarak özel tasarlanır. Dalgaboyuna veya açıya bağlı yansıyan ışığın şiddet spektrasında keskin yüzey plazmon rezonansı eğrileri elde edebilmek için kırınım ağı parmaklarının periyodisite, yüzey profili, derinlik ve yüzde genişliği gibi geometrik parametreler ile üst metal tabakanın dispersiyon ve kalınlığı gibi malzeme özellikleri dikkatlice seçilmelidir. İlk olarak, yüzey plazmon rezonansı kırınım ağlarının sözkonusu geometrik ve malzeme parametreleri RCWA metoduyla sayısal olarak optimize edildi. Onlar mertebesinde açısal kalite faktörlerinin erişilebilir olduğu gösterildi. İyi tanımlanmış kırınım ağı yapılarının nanofabrikasyonu için çeşitli litografik yöntemler (nanobaskı, elektron ışını ve optik litografi) kullanıldı. Spektroskopik elipsometri ile alınan p-polarize yansıyan ışık şiddeti ölçümlerinin sayısal hesaplarla oldukça uyumlu sonuçlar verdiği görüldü. Yüzey plazmon polaritonu uyarımının polarizasyona bağlılığını göstermek için spektroskopik tarama verilerine de ayrıca yer verildi.

Bütün bu yüksek açısal kalite faktörlü kırınım ağı yapıları elde edebilme gayreti açısal yerdeğiştirme tespit şemasının hassasiyetini artırmaya yöneliktir. Bu şemada, kırınım ağı yapısının polarizasyon düzlemindeki açısal konumu, yansıyan ışığın fotodetektördeki sinyali üzerinden tespit edildi. Uyarım ışığının dalga cephesi parametrelerine ve fotodetektör gürültüsüne bağlı hassasiyet analizi yapıldı.

Sözkonusu açısal yerdeğiştirme tespit prensibine dayanan MEMS yerdeğiştirme algılayıcı tasarımları geliştirildi. Basitçe, yüzey plazmon rezonans kırınım ağı yapıları bilindik mikrozarların üzerine aktarıldı. İki çeşit özel mikrozar tasarlandı: kırınım ağlı mikrodirsekler (tek taraftan bağlı) ve kırınım ağlı mikroköprüler (iki taraftan bağlı). Bu aygıtlar kırınım ağı nanofabrikasyonu prosedürlerine ilaveten iyi bilinen yüzey mikroişleme aşamalarıyla üretildi. Mekanik rezonans frekansları, bükülgen mod şekilleri ve efektif yay sabitleri analitik, sayısal ve deneysel olarak çıkarıldı. Ek olarak, nano-G gürültü seviyesinde plazmonik okumalı bir MEMS ivmeölçer tasarımı sunuldu. Mikromekanik yerdeğiştirme algılaması için kurulan bir deneysel konfigürasyon anlatıldı. Bu çalışmanın sonuçlarına göre, plazmon rezonansının ve mikrozar tipi algılayıcıların hassasiyetini birleştiren yeni algılayıcı dizileri benzeri görülmemiş performans sağlayabilirler.

Anahtar kelimeler: Plazmonik, Kırınım Ağı Kuplajlı Yüzey Plazmon Rezonansı, MEMS Algılayıcılar, Mikromekanik Yerdeğiştirme Tespiti

Acknowledgement

I would like to express my deepest gratitude to my supervisor Prof. Salim Çıracı and co-supervisor Prof. Aykutlu Dâna for their invaluable guidance, support and encouragement.

I wish to express my special thanks to Prof. Mehmet Bayındır for his sincere collaboration and instrumental support.

I would like to thank to Prof. Mustafa Özgür Güler for kindly introducing us his laboratory facilities.

I owe thanks to Sencer Ayas, Ozan Aktaş, Kurtuluş Abak, Özlem Şenlik, Handan Acar, Okan Öner Ekiz, Koray Mızrak, Burkan Kaplan, Dr. Mecit Yaman, Mustafa Güler, Burak, Dr. Necmi Bıyıklı, Adem Yıldırım, Hülya Budunoğlu, Yavuz Nuri Ertaş, Can Koral, Seydi Yavaş, Mutlu Erdoğan, Alper Bayrı, Kemal Gürel, Mustafa Ürel, Güneş Kaya, Özlem Köylü, Dr. Abdullah Tülek, Dr. Hakan Deniz, Ahmet Unal, Mehmet Kanık, Tural Hudiyev, Levent Budunoğlu, Hamit Kalaycıoğlu, Bülent Öktem, Kıvanç Özgören, and to all UNAM family.

I appreciate the motivation and moral support of my precious friends Serkan Sonel, Yasin Karadağ, Osman Pamuk, Gökhan Akçay and Murat Ak.

I gratefully acknowledge Advanced Research Laboratory and TUBITAK.

Dedicated to my lovely
family and Aziz

Table of Contents

List of Figures

List of Tables

Chapter 1

Introduction

In electromechanical sensing applications, physical stimuli is detected by measuring the motion or displacement response of the mechanical element.[1] The displacement of the element is detected by various detection techniques including interferometry,[2-7] optical beam deflection,[8-9] piezoresistive,[10] electrostatic [11] and magnetic [12] based schemes. In optical methods, either phase or intensity of the light is modulated by the deflection. Phase modulation or interferometry measurements utilize interference of reference and reflected beams from the mechanical element in motion. In Michelson interferometry, a coherent laser beam is split into two as reference and sample beams. The beam reflecting from the sample interferes with the beam reflecting from the reference mirror.[2] In Fabry-Perot interferometry, an optical cavity is formed within the sacrificial gap of the mechanical element whereas in fiber optic interferometry a micron-sized cavity is formed between the cleaved end of a single-mode optical fiber and the cantilever.[3-5] In interdigital cantilever based optical interferometry, interference takes places between the reflected diffraction orders from moving and support interleaved fingers.[7] Intensity modulation methods, on the other hand, measure the reflected intensity change depending on the displacement of the moving element with respect to the optical spot. In optical beam deflection detection, the displacement of a cantilever is measured by detecting the deflection of a laser beam reflected from the backside of the cantilever using a position sensitive detector.[8,9] Optical beam deflection technique yields high sensitivities comparable with the interferometry based detection schemes.[13] All these introduced optical displacement detection methods are basically limited by the diffraction and photon shot noise.

In this study, we introduce a new optical displacement detection scheme based on surface plasmon resonance. The most common surface plasmon based sensing methods facilitate the refractive index sensitivity of the coupling angle, excitation wavelength, intensity, phase or polarization.[14] Here, use of coupling angle itself for intensity modulation is offered and found to yield high resolution angular displacement detection. Grating coupling is preferred as the surface plasmon excitation mechanism due to easy adaptability to the *microelectromechanical systems* (MEMS). MEMS devices particularly designed for grating coupling are fabricated and characterized. A high performance accelerometer design is presented and analyzed.

Our contributions can be summarized as follows

1. Development of a plasmon resonance based deflection readout scheme for single and array type MEMS devices. This method is shown to be highly sensitive. We also analyze the performance of the readout scheme under different illumination conditions, for various illuminating spectral distributions and focusing settings. Our approach is important for performance estimation of optically detected deflection or displacement sensor arrays.
2. Process development for fabrication of MEMS structures with plasmonic readout, using techniques such as optical and electron beam lithography, nanoimprint lithography, PDMS molding, dry/wet etching. Application of the process to fabrication of prototype devices.
3. Design of a MEMS accelerometer with plasmon resonance based readout. The performance of the device is estimated to be Brownian motion limited, and with proper design that is within our fabrication capabilities, nano-g accelerations are shown to be attainable. A simple prototype accelerometer using the design was shown to operate, although final devices remained as designs.
4. Two peer-reviewed articles have been published during the course of this thesis and a final article is in preparation.

Organization of the thesis is as follows. In Chapter 2, electromagnetic theory of surface plasmons is briefly introduced. Grating coupling mechanism as of our interest is explained. In Chapter 3, our efforts on obtaining efficient grating couplers are presented. In Chapter 4, proposed SPR based angular displacement detection scheme is analyzed. In Chapter 5, design, fabrication and characterization steps of MEMS displacement sensors are explained. In addition, design and sensitivity analysis of a MEMS accelerometer is presented.

Chapter 2

Grating Coupled Surface Plasmon Resonance

In this chapter, the theoretical solution of surface plasmons is derived within the framework of Maxwell's equations and the Drude model of metals. Grating coupling scheme is discussed as the surface plasmon excitation mechanism of our concern.

2.1 Surface Plasmons

Surface plasmons are charge density oscillations propagating along the metal-dielectric interfaces. The free electrons of the metal respond collectively and resonantly to an excitation light wave or an incident electron. These variations of surface charge density corresponds to an electromagnetic field at the surface which decays exponentially in both media.

In a macroscopic media and without source terms, Maxwell's equations take the form [15]

$$\begin{aligned} &\nabla.\mathbf{D} = 0 \\ &\nabla.\mathbf{B} = 0 \\ &\nabla \times \mathbf{E} = -\frac{1}{c}\frac{\partial \mathbf{B}}{\partial t} \\ &\nabla \times \mathbf{H} = \frac{1}{c}\frac{\partial \mathbf{D}}{\partial t} \end{aligned} \tag{2.1}$$

where $\mathbf{D}$ is the electric displacement, $\mathbf{B}$ is the magnetic flux density, $\mathbf{E}$ is the electric field, $\mathbf{H}$ is the magnetic field and c is the speed of light. Assuming materials with linear polarization and magnetic responses in respect to the external fields, the electric and magnetic quantities are interconnected by the material equations as

$$\begin{aligned} &\mathbf{D} = \varepsilon_0 \varepsilon(\omega)\mathbf{E} \\ &\mathbf{B} = \mu_0 \mu(\omega)\mathbf{H} \end{aligned} \tag{2.2}$$

where ε_0 is the electric permittivity of free space, $\varepsilon(\omega)$ is the dielectric constant, μ_0 is the magnetic permeability and $\mu(\omega)$ is the relative permeability. $\varepsilon(\omega)$ and $\mu(\omega)$ are the complex functions of the angular frequency ω of the exciting field. Hence, Maxwell's equations can be solved by electric plane waves as

$$\mathbf{E}(\mathbf{r},t) = \mathbf{E}_0 e^{i(\mathbf{k}.\mathbf{r}-\omega t)} \tag{2.3}$$

where $\mathbf{r}$ is the position in space, t is the time, $\mathbf{E}_0$ is the electric field amplitude and $\mathbf{k}$ is the wavevector. $\mathbf{E}_0$ is always orthogonal to $\mathbf{k}$ which is along the direction of propagation. The electric and the magnetic plane waves are interconnected via

$$\begin{aligned} \mathbf{E}(\mathbf{r},t) &= -\frac{c}{\omega\varepsilon_0\varepsilon(\omega)}\mathbf{k}\times\mathbf{H}(\mathbf{r},t) \\ \mathbf{H}(\mathbf{r},t) &= -\frac{c}{\omega\mu_0\mu(\omega)}\mathbf{k}\times\mathbf{E}(\mathbf{r},t) \end{aligned} \tag{2.4}$$

The wavevector and the angular frequency are dependent of each other by the photonic dispersion relation as

$$\frac{\omega^2}{|\mathbf{k}|^2} = \frac{1}{\varepsilon_0\varepsilon(\omega)\mu_0\mu(\omega)} \tag{2.5}$$

Assuming the media is nonmagnetic ($\mu(\omega)=1$) and with the identity $c^2 = \frac{1}{\mu_0\varepsilon_0}$, the magnitude of the wavevector can be expressed as

$$|\mathbf{k}| = \omega\sqrt{\mu_0\varepsilon_0\varepsilon(\omega)} = \frac{\omega}{c}\sqrt{\varepsilon(\omega)} \tag{2.6}$$

The dielectric function of a metal as a function of the angular frequency of the external applied field is given by the Drude model [16] as

$$\varepsilon(\omega) = 1 - \frac{\omega_p^2}{\omega^2 + i\dfrac{\omega}{\tau}} \tag{2.7}$$

where ω_p is the plasma frequency and τ is the mean free time between the mutual collisions of the electrons. The plasma frequency is given by

$$\omega_p = \frac{n_e e^2}{\varepsilon_0 m_e} \tag{2.8}$$

where n_e is the electron density, e is the electron charge and m_e is the effective electron mass. Eq.2.7 can be applied frequencies lower than the plasma frequency. This model works well for a spectral range from visible to microwave wavelengths.

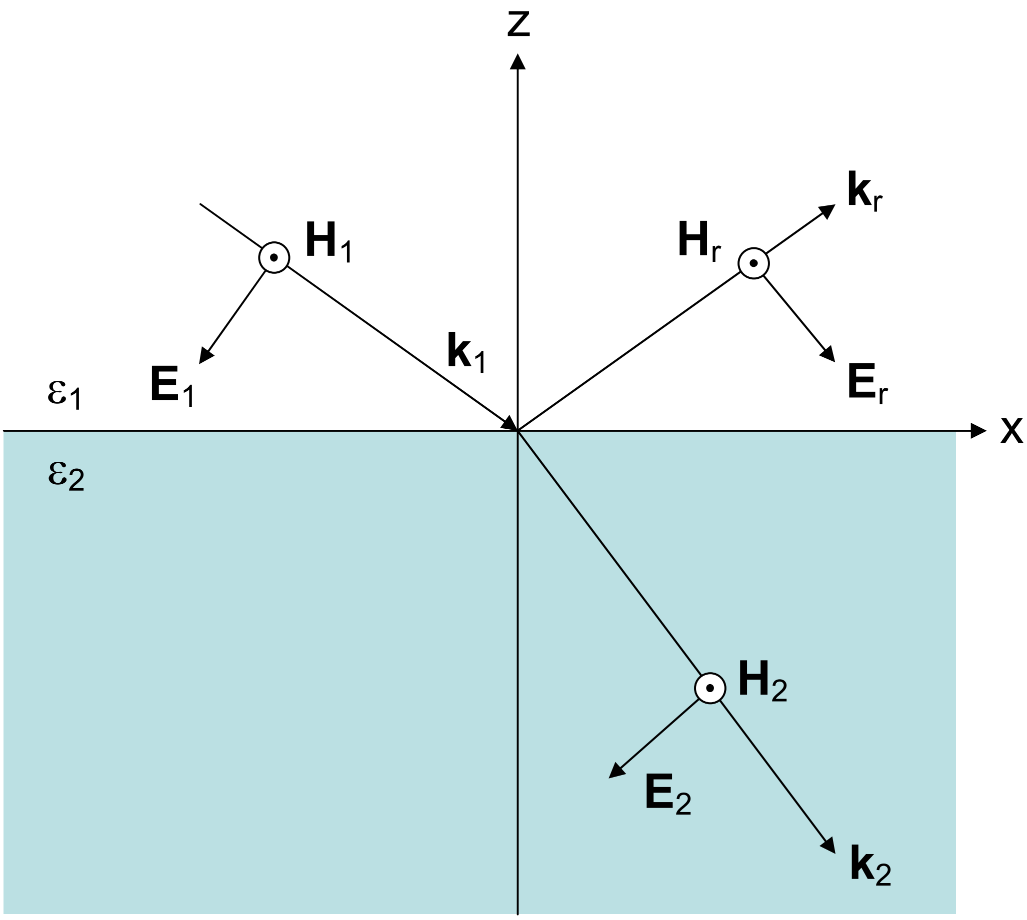

Figure 2.1: An electromagnetic wave at an interface

We now focus on the surface plasmon solutions at a metal-dielectric interface. Surface charges can only be induced by an electric field component along the z-axis (Fig.2.1). Therefore only p-polarized wave can excite surface plasmons. Since surface plasmons are known to be propagating along the interface and evanescently confined in the perpendicular direction, the electric field components in both media can be formulated as

$$\begin{aligned}
\mathbf{E}_{x1} &= E_{x1} e^{i(k_{x1}x + k_{z1}z - \omega t)} \hat{\mathbf{x}} \\
\mathbf{E}_{y1} &= 0 \\
\mathbf{E}_{z1} &= E_{z1} e^{i(k_{x1}x + k_{z1}z - \omega t)} \hat{\mathbf{z}} \\
\mathbf{E}_{x2} &= E_{x2} e^{i(k_{x2}x - k_{z2}z - \omega t)} \hat{\mathbf{x}} \\
\mathbf{E}_{y2} &= 0 \\
\mathbf{E}_{z2} &= E_{z2} e^{i(k_{x2}x - k_{z2}z - \omega t)} \hat{\mathbf{z}}
\end{aligned} \tag{2.9}$$

where the indices 1 and 2 refer to the half-spaces ($z > 0$) and ($z < 0$), respectively. The k_{xi} and k_{zi} are the respective x and z components of the total wavevector $\mathbf{k}_i$. From Eq.2.4, the magnetic field components can be found as

$$\begin{aligned}
\mathbf{H}_{x1} &= 0 \\
\mathbf{H}_{y1} &= H_{y1} e^{i(k_{x1}x + k_{z1}z - \omega t)} \hat{\mathbf{y}} \\
\mathbf{H}_{y1} &= 0 \\
\mathbf{H}_{x2} &= 0 \\
\mathbf{H}_{y2} &= H_{y2} e^{i(k_{x2}x - k_{z1}z - \omega t)} \hat{\mathbf{y}} \\
\mathbf{H}_{y2} &= 0
\end{aligned} \tag{2.10}$$

From the continuity condition, the components of $\mathbf{E}$ and $\mathbf{H}$ parallel to the interface have to be equal to each other

$$\begin{aligned}
E_{x1} &= E_{x2} \\
H_{y1} &= H_{y2}
\end{aligned} \tag{2.11}$$

It is followed by the continuity of wavevectors

$$k_{x1} = k_{x2} = k_x \tag{2.12}$$

Applying these constraints, Eq.2.4 becomes

$$\begin{aligned}
k_{z1} H_{y1} &= \frac{\omega}{c} \varepsilon_1 E_{x1} \\
k_{z2} H_{y2} &= -\frac{\omega}{c} \varepsilon_2 E_{x2}
\end{aligned} \tag{2.13}$$

In the non-trivial case, Eq.2.13 yields

$$\frac{k_{z1}}{k_{z2}} = -\frac{\varepsilon_1}{\varepsilon_2} \tag{2.14}$$

This relation can only be met if the dielectric constants of the mediums have opposite signs. This is why surface plasmons exist at only metal-dielectric interfaces. Using Eq.2.6, k_{zi} can be expressed as

$$k_{zi}^2 = (\frac{\omega}{c})^2 \varepsilon_i - k_{xi}^2 \tag{2.15}$$

Taking square of Eq.2.14 and using Eq.2.12, we are led to the plasmonic dispersion relation

$$k_x = \frac{\omega}{c}\sqrt{\frac{\varepsilon_1 \varepsilon_2}{\varepsilon_1 + \varepsilon_2}} \tag{2.16}$$

At a metal-dielectric interface, $\varepsilon_1 = \varepsilon_d$ is a real number for the dielectric and $\varepsilon_2 = \varepsilon_m$ is a complex number for the metal. Metals have a negative real part and a smaller positive imaginary part ($\varepsilon_m'' < |\varepsilon_m'|$). Thus k_x and k_z become complex quantities. Substituting the complex wavevectors into Eq.2.9 and Eq.10, we get harmonic and exponentially decaying parts. $\mathbf{E}_x$, $\mathbf{E}_z$ and $\mathbf{H}_y$ fields show evanescent characteristics therefore surface plasmons are considered as damped nonradiative surface waves.

2.2 Grating Coupling Scheme

Neglecting the imaginary component of ε_m, in-plane wavevector k_x of a surface plasmon is found to be always greater than the wavevector of light in air as

$$k_{sp} = \frac{\omega}{c}\sqrt{\frac{\varepsilon_m \varepsilon_d}{\varepsilon_m + \varepsilon_d}} \geq k_{light,air} = \frac{\omega}{c}\sqrt{\varepsilon_d} \tag{2.17}$$

As shown in Fig.2.2, there is no intersection of photonic and plasmonic dispersion curves except the origin which indicates that photons and plasmons with the same energy of $\hbar\omega$ have different in-plane momentums of $\hbar k_x$. However, for an interaction between photons and plasmons to take place, it is a fundamental requirement to have both same energy and momentum due to the conservation principles of both energy and momentum. If, somehow, energy and momentum match condition is satisfied, surface plasmons are excited by the light. The most common methods for optical excitation of surface plasmons are prism and grating coupling schemes.[17-19] In this study, we deal with the grating coupling mechanism.

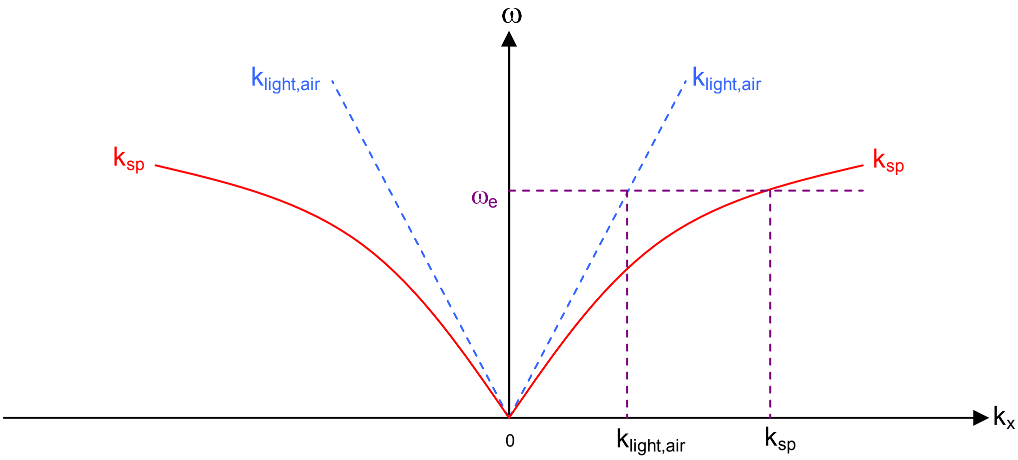

Figure 2.2: Photonic and plasmonic dispersion relations.

When a light wave with the wavevector of $\mathbf{k}_{inc}$ is incident upon the surface of a grating, diffraction occurs. In-plane wavevector of the diffracted light $\mathbf{k}_{diff,x}$ is given by

$$\mathbf{k}_{diff,x} = \mathbf{k}_{inc,x} + m\mathbf{G} \tag{2.18}$$

where m is an integer denoting the diffraction order and $\mathbf{G}$ is the grating vector along the x direction, subject to the condition that the magnitude of the wavevector remains same

$$|\mathbf{k}_{diff}| = |\mathbf{k}_{inc}| \tag{2.19}$$

if the diffracted light stays in the same index medium.[20] The magnitude of the grating vector is given by

$$|\mathbf{G}| = \frac{2\pi}{\Lambda} \tag{2.20}$$

where Λ is the grating period. Surface plasmons are excited when the in-plane wavevector of the diffracted light $\mathbf{k}_{diff,x}$ is equal to the wavevector of the surface plasmons $\mathbf{k}_{sp}$:

$$k_{inc,x} + m\frac{2\pi}{\Lambda} = k_{sp} \tag{2.21}$$

Since the surface profile has translational symmetry, the plasmonic dispersion relation has also translational symmetry:

$$\omega(\mathbf{k}_x) = \omega(\mathbf{k}_x + m\mathbf{G}) \tag{2.22}$$

Figure 2.3 shows the plasmonic dispersion relation for grating coupling.

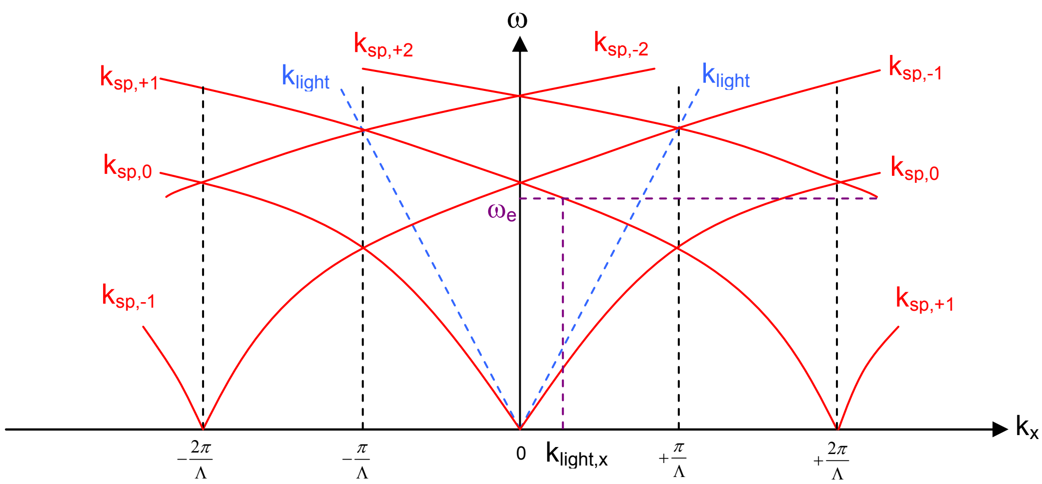

Figure 2.3: The plasmonic dispersion relation for grating coupling.

Chapter 3

Optimization, Fabrication and Characterization of SPR Gratings

Efficient coupling of excitation light to surface plasmons is desirable in SPR based sensing applications. This chapter outlines our effort on obtaining high-efficient grating couplers both numerically and experimentally.

3.1 Optimization of Gratings

Optimization of grating couplers via numerical methods including finite element method (FEM) [21], finite-difference time domain (FDTD) [22] dyadic Green's tensor method and rigorous coupled wave analysis (RCWA) [23] has been discussed in the previous works. RCWA is proposed as a successful and accurate method for the analysis of the diffraction of electromagnetic waves by periodic structures. [24] In this study, we introduce our results on the numerical optimization of silver coated gratings in air medium based on RCWA. Complex permittivity data is supplied from Palik's Handbook of Optical Constants of Solids. [25]

3.1.1 Geometric Parameters

Main geometric properties of a grating to be optimized are periodicity, surface profile, groove depth and duty cycle.

- **Periodicity:** Surface plasmon excitation wavelength λ_e and resonance angle θ_R pair is approximately derived from the grating coupling equation depending on the grating period Λ and dielectric constants of the surrounding dielectric media, ε_d and the metallization, ε_m. In the case of a silver grating in air medium, Λ is found as 740 nm and 545 nm for the $+1^{st}$ and -1^{st} diffracted orders, respectively, for λ_e=633 nm and θ_R=8.8 deg as shown in Fig.3.1. Due to the fabrication considerations which are explained in Chapter 3.2.1, Λ is set as 740 nm for the following numerical calculations.

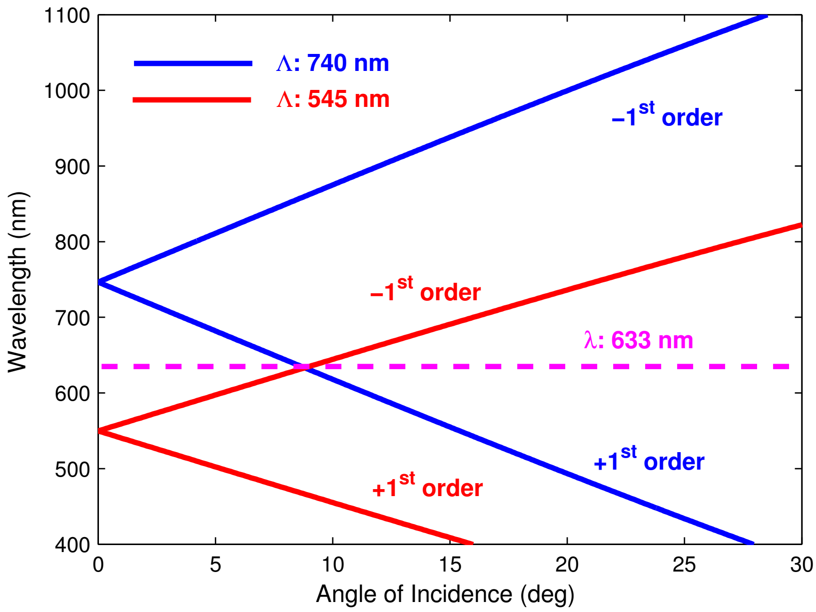

Figure 3.1: Dispersion curves of a silver coated grating in air medium for grating periods of Λ=740 nm and Λ=545 nm

- **Surface profile:** Sinusoidal and non-sinusoidal gratings are simulated in order to reveal the effect of spatial harmonics on the reflectivity spectra with respect to the angle of incidence. Grating coupling equation estimates resonance angles as $\theta_{R,1}$=8.8 and $\theta_{R,2}$=44.6 degrees for the first and second spatial harmonics, respectively, at SPP excitation wavelength of 633 nm for a silver grating with Λ=740 nm (Fig.3.2). More accurate resonance angles are obtained by RCWA as $\theta_{R,1}$=10.3 and $\theta_{R,2}$=42 degrees (Fig.3.3). Since sinusoidal grating has no higher spatial harmonics and lamellar grating has no even higher spatial harmonics, there exists no resonance curve around $\theta_{R,2}$=42 deg. However, we see plasmonic resonances for sawtooth and arbitrarily defined gratings around $\theta_{R,2}$=42 deg due to the existence of even spatial harmonics in addition to odd spatial harmonics. Indeed, we deal with the sharpness of the resonance curves and use angular quality factor as a measure of the sharpness which is defined as the ratio of the resonance angle and FWHM angle. Sinusoidal, sawtooth and arbitrary gratings are found to have angular Q-factors varying between 17 and 22 whereas lamellar grating has a lower angular Q-factor around 9.

  Higher spatial order resonance curves offer additional resonance angles at a constant excitation wavelength. However, angular Q-factor reduction due to the intersection and broadening of the resonance curves at an interval of certain excitation wavelengths should be carefully treated (Fig.3.4). For the case of the arbitrary grating which has both even and odd spatial harmonics, angular Q-factor decreases from 13 to 9 for the excitation wavelengths of 550 nm and 529 nm, respectively (Fig.3.5). On the other hand, angular Q-factor slightly reduces to 12.24 for the excitation wavelength of 522 nm even the peak reflectivity rises up above 0.64.

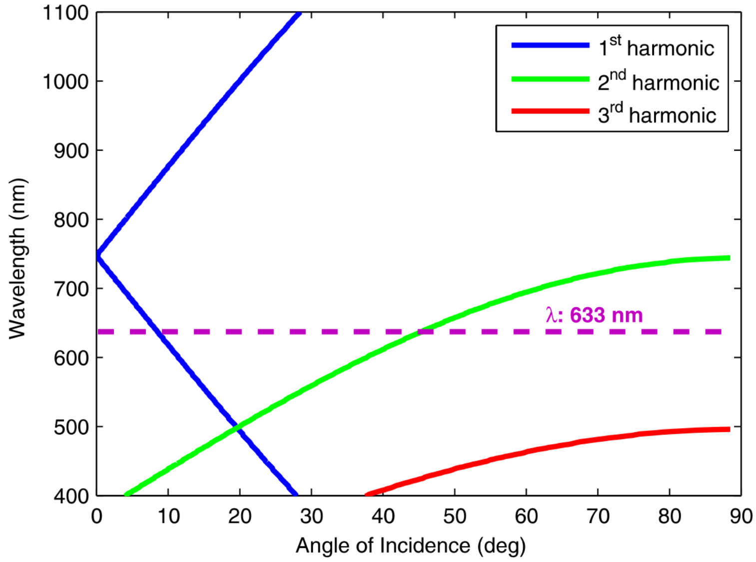

Figure 3.2: Dispersion curves of the first and higher spatial harmonics of a silver grating in air medium for grating period of Λ=740 nm

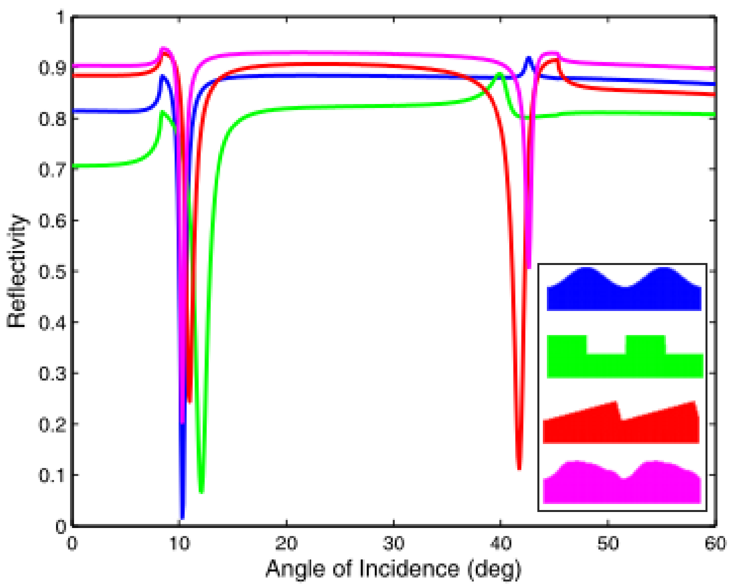

Figure 3.3: Reflectivity spectrum with respect to the angle of incidence for various grating profiles.

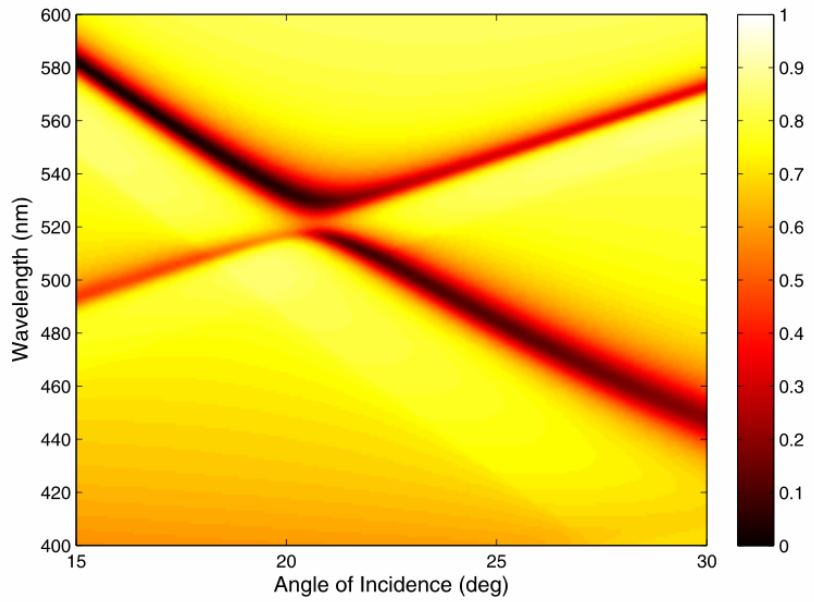

Figure 3.4: Dispersion curves of an arbitrary grating which has both even and odd spatial harmonics. (Λ=740 nm)

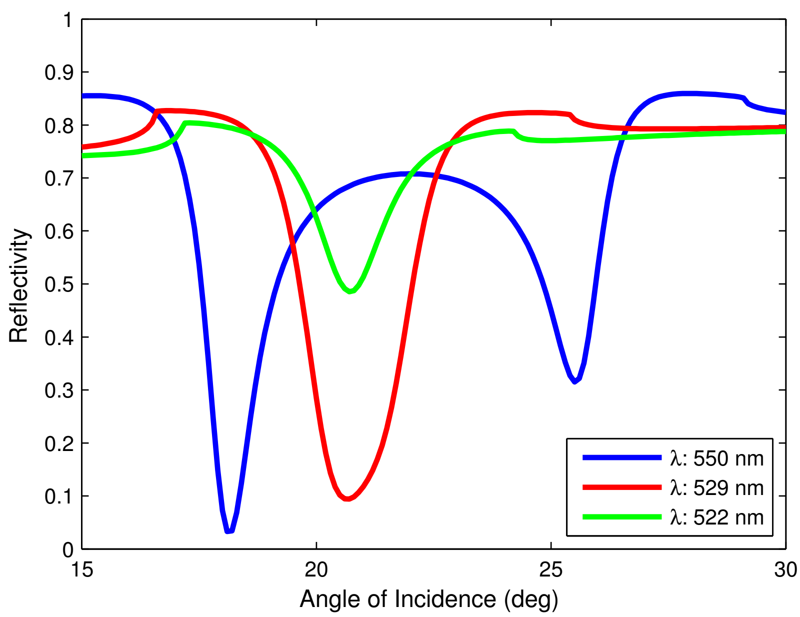

Figure 3.5: Angular Q-factor reduction due to the intersection and broadening of the first and second spatial harmonic resonance curves.

- **Groove depth:** RCWA simulations reveal that peak reflections strongly depend on the groove depth (Fig.3.6). 45 nm depth is found as the optimal depth for a sinusoidal silver grating in air. Substantial Q-factor reduction as much as 60%'s is observed as the groove depth is set from 45 nm to 90 nm (Fig.3.7).

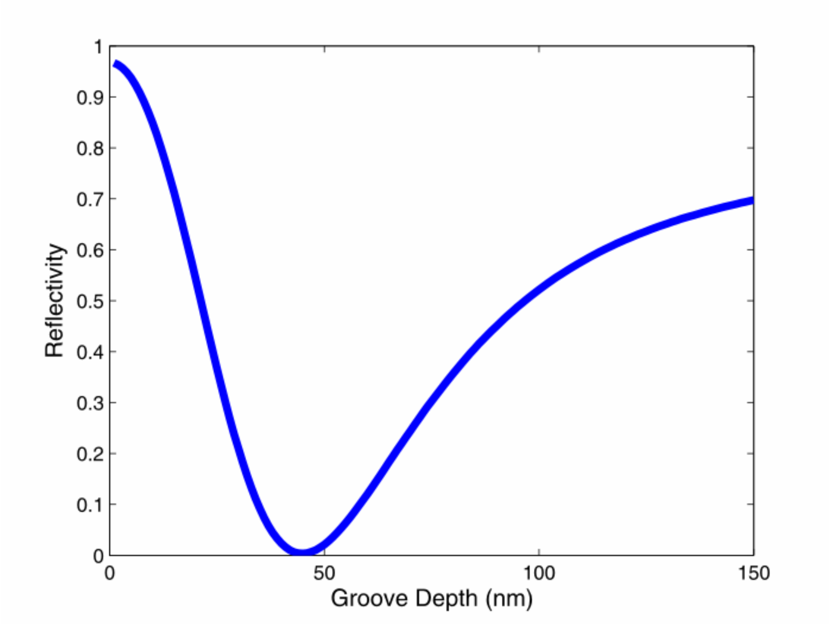

Figure 3.6: Peak reflectivity as a function of the groove depth. (λ_e=633 nm, Λ=740 nm)

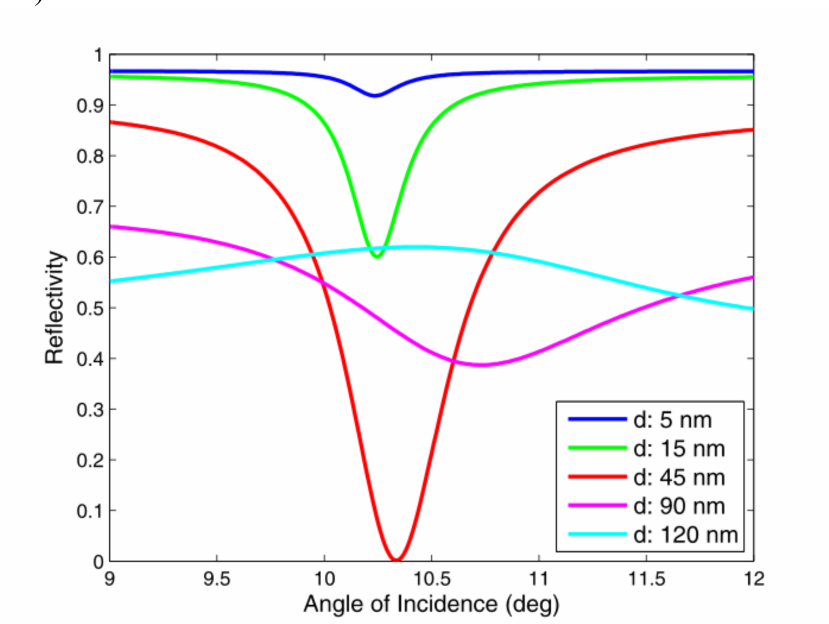

Figure 3.7: Reflectivity spectrum with respect to the angle of incidence for various groove depths.

- **Duty cycle:** Duty cycle (ratio of the ridge width to the grating period) of a lamellar grating is also found to be as a critical parameter as the groove depth (Fig.3.8). Duty cycles around 50% are found to be optimal. Resonance angle shifts are observed in addition to the angular Q-factor reduction depending on the duty cycle (Fig.3.9).

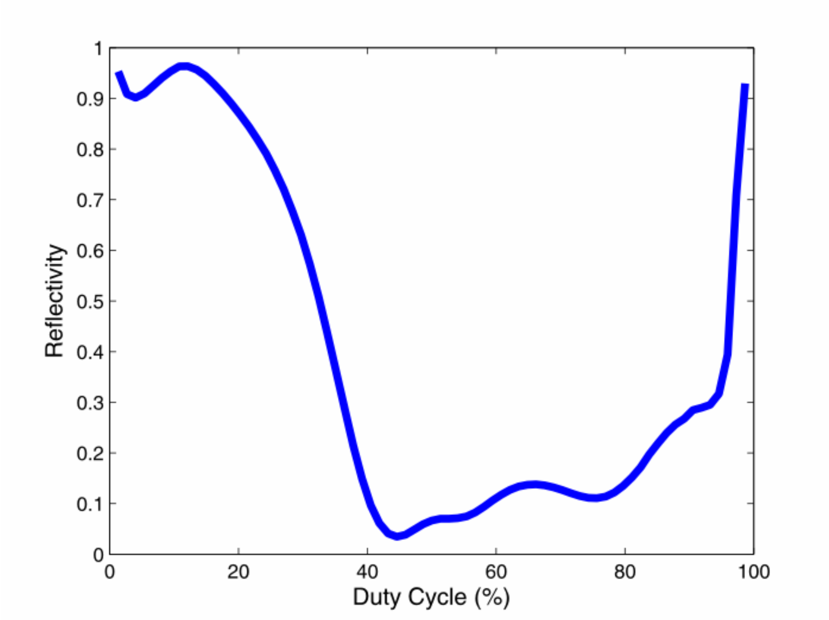

Figure 3.8: Peak reflectivity as a function of the duty cycle. (λ_e=633 nm, Λ=740 nm)

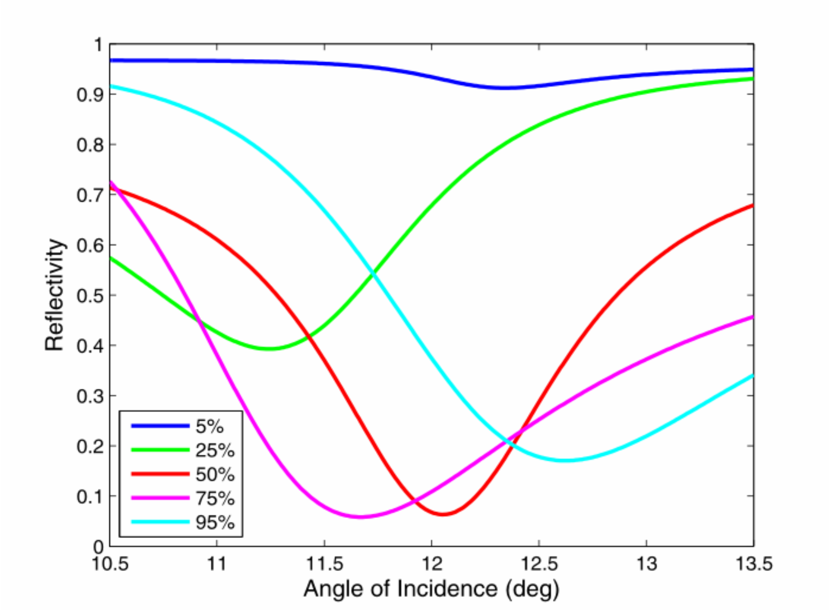

Figure 3.9: Reflectivity spectrum with respect to the angle of incidence for various duty cycles.

3.1.2 Metallization Parameters

Main metallization parameters to be optimized are thickness and material.

- **Thickness:** Metal layers are coated on gratings made of a different material. As the metal film gets thinner, optical properties of the sublayer may not be neglected anymore. Normalized intensities of reflectance, transmittance and absorbance as a function of the thickness of silver coating on a sublayer with the refractive index of n_s=1.45 are numerically calculated (Fig.3.10). As the non-reflected intensity is transmitted rather than absorbed due to thinner metallization, broadening in the reflected intensity curve is observed (Fig.3.11 and Fig.3.12). Thicknesses above 100 nm are found to be safe for silver coated gratings with 60 nm depth.

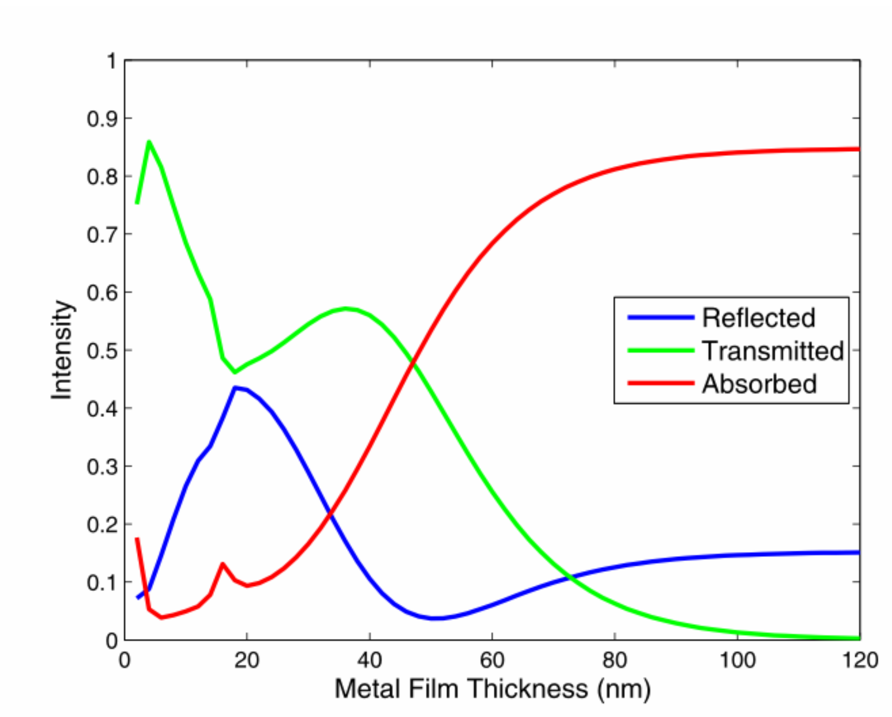

Figure 3.10: Normalized intensities of reflectance, transmittance and absorbance as a function of the thickness of silver coating. (λ_e=633 nm, Λ=740 nm)

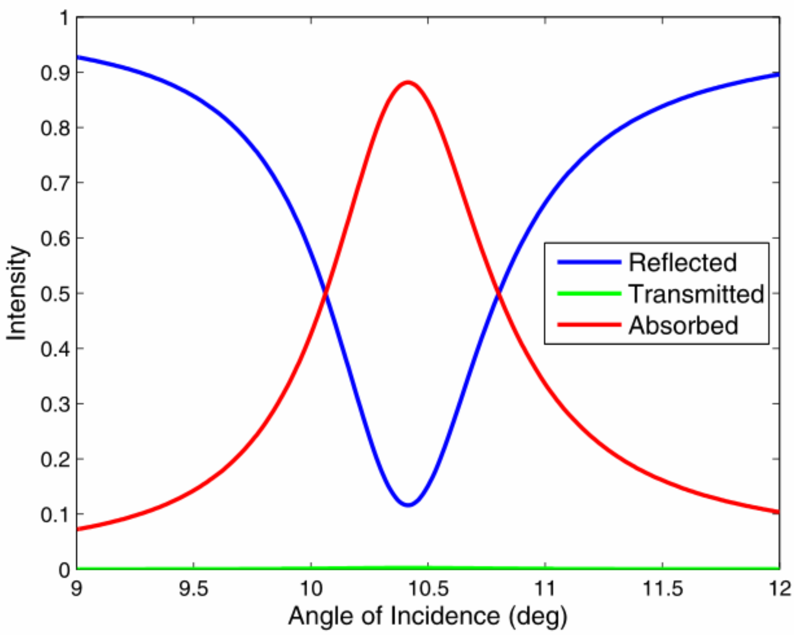

Figure 3.11: Normalized intensities of reflectance, transmittance and absorbance with respect to the angle of incidence for a silver coated grating with the thickness of t_{Ag}=120 nm on a sublayer with the refractive index of n_s=1.45.

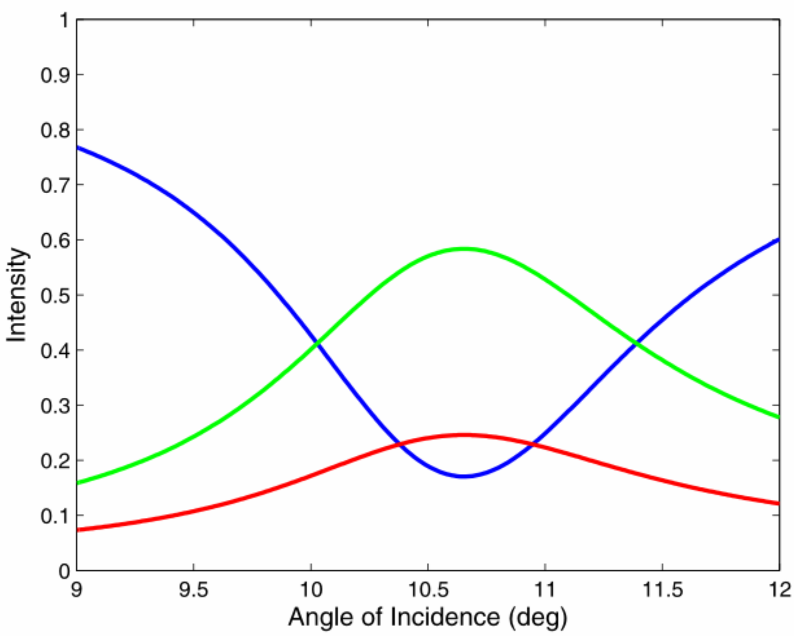

Figure 3.12: Normalized intensities of reflectance, transmittance and absorbance with respect to the angle of incidence for a silver coated grating with the thickness t_{Ag}=35 nm on a sublayer with the refractive index of n_s=1.45.

- **Material:** Material of the metallization is obviously one of the most fundamental parameters of grating coupled SPR as can be deduced from grating coupling equation. At excitation wavelength of 633 nm, silver coating is found to yield the sharpest resonance curves as compared with the aluminum and gold coatings (Fig.3.13).

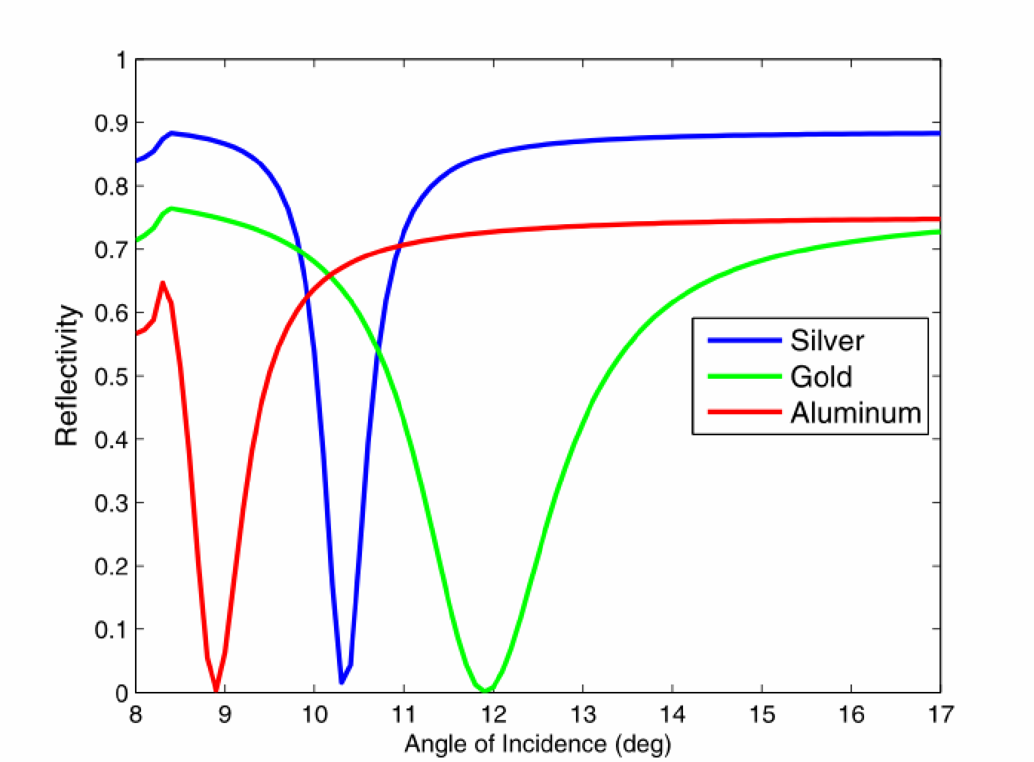

Figure 3.13: Reflectivity spectrum with respect to the angle of incidence for various metal coatings. (λ_e=633 nm, Λ=740 nm)

3.2 Fabrication of Gratings

3.2.1 Nanoimprint Lithography

Quasi-sinusoidal gratings are fabricated using nanoimprint lithography as shown schematically in Fig.3.15. We prepare master molds from commercial optical discs by applying some chemical and physical procedures [26]. Corrugations near the edges of such discs are well approximated by gratings with a period of Λ=1540 nm for CD-R, Λ=740 nm for DVD-R and Λ=340 nm for Blu-Ray. The rewritable discs generally use a hard chalcogenide material as the recording medium (CD-RW and DVD-RW) and Blu-Ray write-once discs also use a multilayer hard coating. However, the write-once CD-R and DVD-R discs use a dye layer as the recording medium that can be dissolved in weaker solvents. Therefore, we focus on the write-once discs. For the case of the DVD-R discs, due to the thick layers that protect the recording layer, the inner surface was exposed by first mechanically cutting a notch into the side of the disc and then by applying mechanical force to peel the two sides apart. The initial cut provides a location for separation, which can be initiated by a sharp cutter. After peeling off the top surface, the dye layer was washed repeatedly in isopropanol. This procedure was observed not to change the disc corrugation but completely remove the dye. After cleaning, a 4:1 mixture of isopropanol and acetone was used to etch the grating to the desired depth. Typical etch times were from 10 seconds to a few minutes. Slight agitation during etching was observed to be important for uniform and repeatable etching. In the case of CD-R, the top protective layer was peeled off by exfoliation using a tape after delineation of the surface with a sharp cutter. The same procedure that was used for the DVD-R was also used for cleaning and etching of the CD-R discs. The effect of etching on the topography of disc surfaces are measured using atomic force microscopy (PSIA XE100) as shown in Fig.3.14.

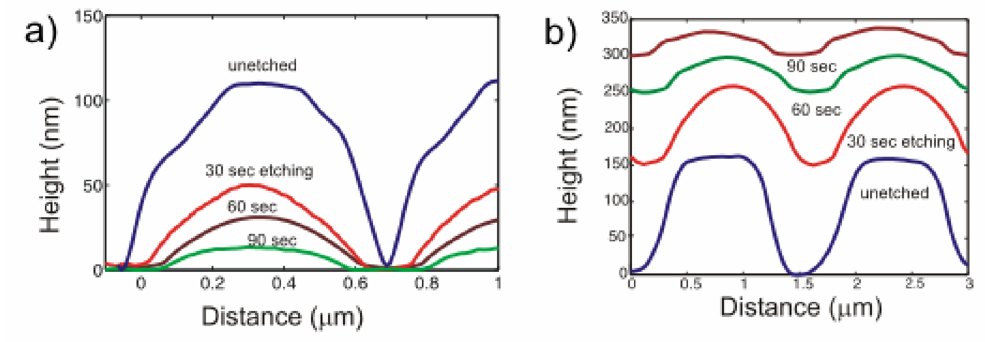

Figure 3.14: Topographic profiles of the gratings obtained by Atomic Force Microscopy as a function of etching time on optical discs. (a) Modified DVD-R disc surface profiles with Λ=740 nm. (b) Modified CD-R disc surface profiles with Λ=1540.

Having modified DVD-R as master mold, liquid polydimethylsiloxane (PDMS) (Sylgard 184, Dow Corning) is poured on and cured at 70 °C during 5 hours (Fig.3.15). After curing, elastomeric stamp is peeled off from the master mold. As the grating material, a photoresist (AZ5214, AZ Electronic Materials) is diluted 1:3 by a photoresist thinner (AZ1500 Thinner, AZ Electronic Materials) and spin-coated at 8000 rpm. Elastomeric stamp is released softly on the thinned photoresist film and hard-baked on the hotplate at 120 ^{o}C about 5 minutes. At last, stamp is mechanically removed from the sample. AFM image of sine-like polymeric grating is shown in Fig.3.16.

Further adjustment of the groove depth to some degree keeping the profile of the polymeric grating almost unchanged is possible (Fig.3.17). Hard-baking at a higher temperature than 120 ^{o}C results deeper gratings. For our case, hard-baking at 180 ^{o}C yields 100 nm depth whereas hard-baking at 120 ^{0}C yields 55 nm depth. In order to get shallower surfaces, diluted isopropanol etch or O_2 plasma treatment may be applied. Groove depth is reduced from 55 nm to 35 nm by 2:1 IPA:DI wet etch for 6 min and 45 nm by reactive ion etching (RIE) O_2 plasma etch for 1 min at 100W RF power. However, wet etching gives smoother surfaces than dry etching.

Unfortunately, polymeric gratings suffer from KOH etch process which has to be used latter to release micromembranes even metal-coated by either sputtering or thermal evaporation. Adding one more step, we have transferred grating patterns from thin polymer film to the underlying SiNx layer by fluorine based reactive ion etching (Fig.3.18). CHF_3:O_2 plasma etches both SiNx and thinned photoresist with a higher etch rate of SiNx. Surface profile of the polymeric grating is almost conserved during the RIE etching until the SiNx sublayer is reached due to the high vertical directionality of RIE etch and low thickness of the photoresist film. As SiNx layer is reached, both photoresist and SiNx layers are etched together. The more photoresist is etched vertically, the more SiNx layer is subject to the plasma etchants laterally. As a result, grating profile is transferred from the polymer to the SiNx layer with depth multiplied by approximately the ratio of the etch rates. AFM images of the resulting SiNx gratings are shown in Fig.3.19. Similar to the previous case, further surface modification is possible to tune the groove depth. 1:2560 HF:DI etch for 10 min reduces the groove depth from 120 nm to 85 nm Fig.3.20.

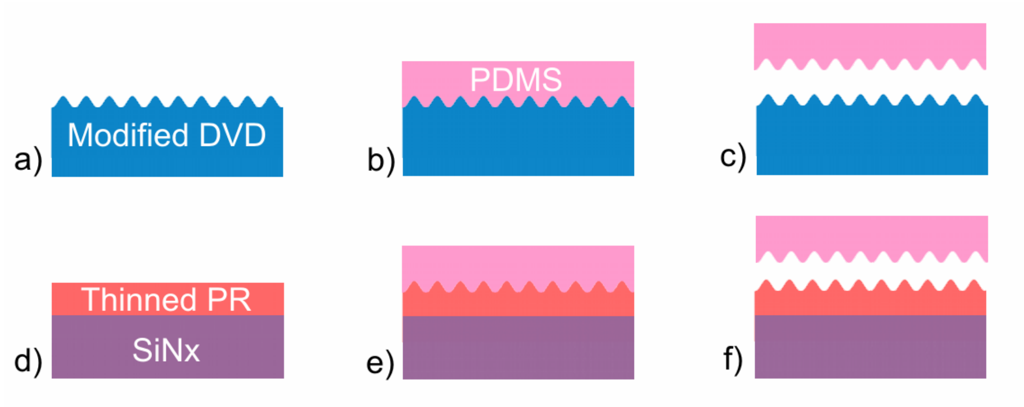

Figure 3.15: Fabrication steps of the polymeric gratings using nanoimprint lithography. (a) Surface modified DVD-R disc with sine-like profile is used as master mold. (b) PDMS is poured on the master mold and cured at 70 ^{0}C for 5h. (c) Cured PDMS is peeled off from the master mold and used as elastomeric stamp. (d) Thinned photoresist is spin-coated on SiNx deposited substrate. (e) Elastomeric stamp is released gently on the thin polymer film and hard-baked to make polymer hardened. (f) Elastomeric stamp is mechanically removed from the sample.

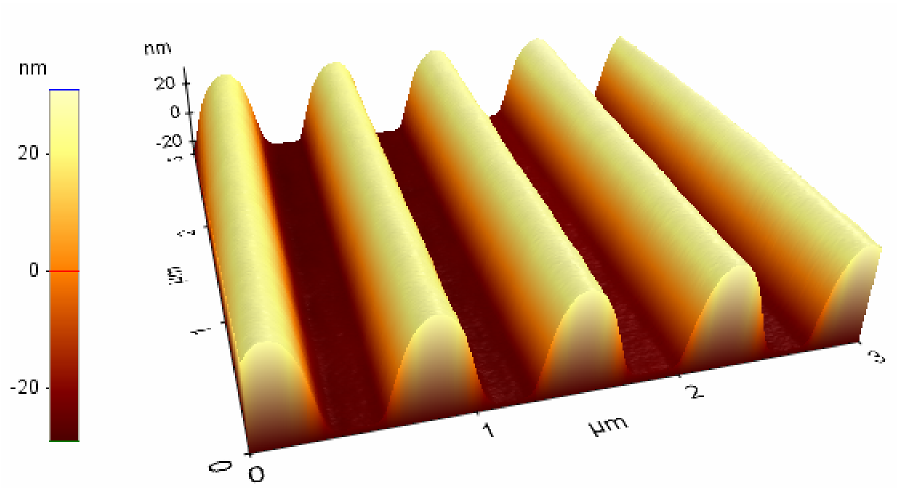

Figure 3.16: AFM topography image of the sine-like nanoimprinted polymeric grating

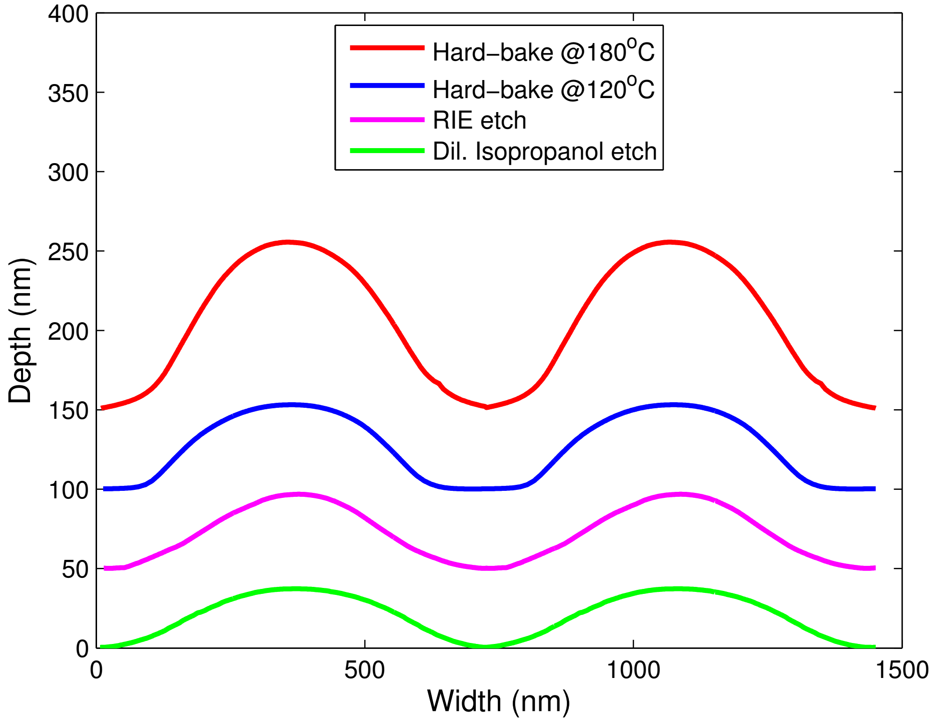

Figure 3.17: Topographic profiles of the polymeric gratings with different groove depths

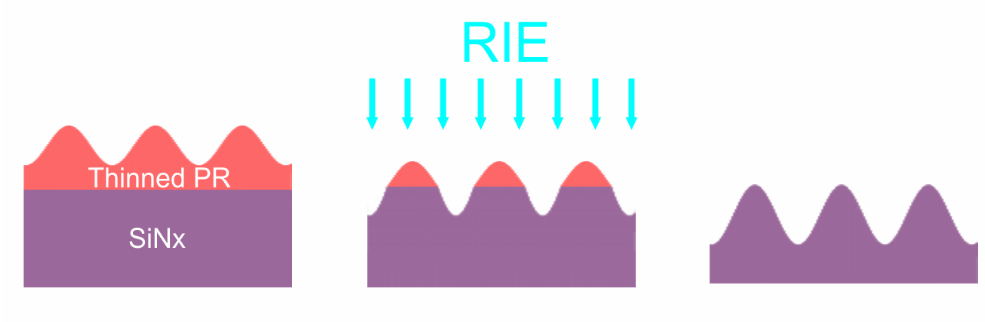

Figure 3.18: Schematic representation of polymer-to-SiNx grating pattern transfer process using fluorine based reactive ion etching

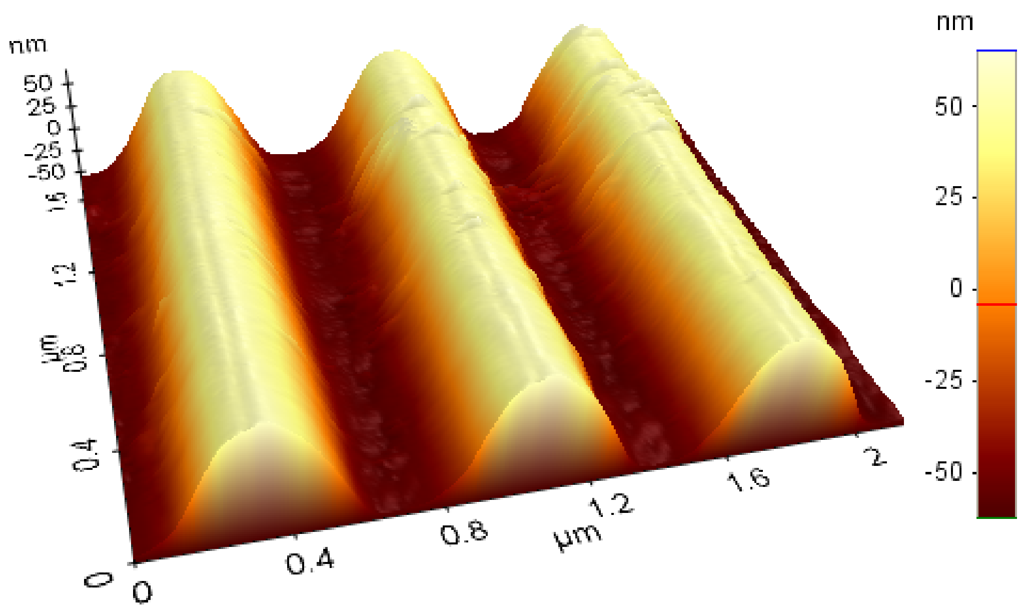

Figure 3.19: AFM topography image of the sine-like SiNx grating

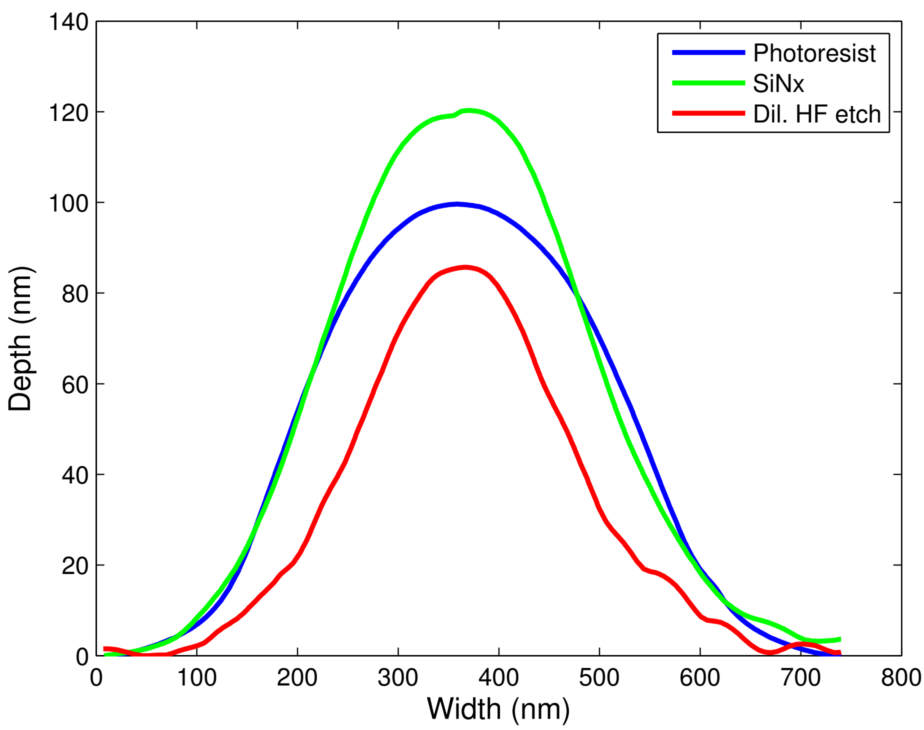

Figure 3.20: Topographic profiles of the polymeric and SiNx gratings

3.2.2 Electron Beam Lithography

Lamellar SiNx gratings are fabricated using electron beam lithography (FEI Nova NanoSEM 600). Two alternative processes are used: (a) Cr etch process and (b) Cr lift-off process (Fig.3.21). At process (a), chromium etch mask is defined by chromium etching. First, 50 nm chromium is sputtered on PECVD (plasma-enhanced chemical vapor deposition) growth SiNx film. Electron beam lithography resist poly (methyl methacrylate) (PMMA) is spin-coated and pre-baked at 180 ^{o}C for 2 minutes. 740 nm period linear gratings are defined by electron beam exposure. PMMA is developed in 1:3 methyl isobutyl ketone (MIBK): isopropyl alcohol (IPA) developer solution. Chromium is wet etched in 1:5 diluted Cr etchant (CR-7S, Cyantek) for 1 min. SiNx is then dry etched by RIE CHF_3:O_2 plasma. Chromium mask is removed at the end and we are left with lamellar SiNx gratings. At process (b), chromium etch mask is defined by lift-off process. First, PMMA is spin coated and pre-baked as in the previous case. After PMMA develop, chromium is sputtered on. PMMA mask is removed in ultrasonic acetone bath. Chromium sputtered on the PMMA are lifted-off and the same RIE etch procedure is followed. It should be noted that lift-off process has superiorities over the other process. First, wall profiles of the Cr mask is undoubtedly better such that Cr mask itself may be used as the grating excluding the RIE etch process. Second, it does not suffer from overetches which may lower the duty cycle. On the other hand, PMMA film has to be sufficiently thicker than the Cr film for the lift-off process to occur. Atomic force microscopy and scanning electron microscopy images of lamellar SiNx gratings fabricated using the second process are shown in Fig.3.21.

Exposure parameters should be optimized on some dummy samples before starting the fabrication of desired structures. Dose matrix process is employed for this purpose. In this process, a matrix of mask elements with steadily increasing exposure dose values is prepared and exposed to a dummy sample. Standard procedures for developing the PMMA are followed and according to the PMMA mask patterns imaged by usual scanning electron microscopy, the best fitting dose values are determined. For our case, at 10 kV beam voltage and 150 pA measured beam current, 100 mJ/cm^2.sec gives the optimal results. Also exposure resolution which is basically limited by the interface electronics between the lithography instrument and the control PC is an important parameter. 20 nm spatial resolution is found to produce satisfactorily smooth grating patterns with Λ=740 nm.

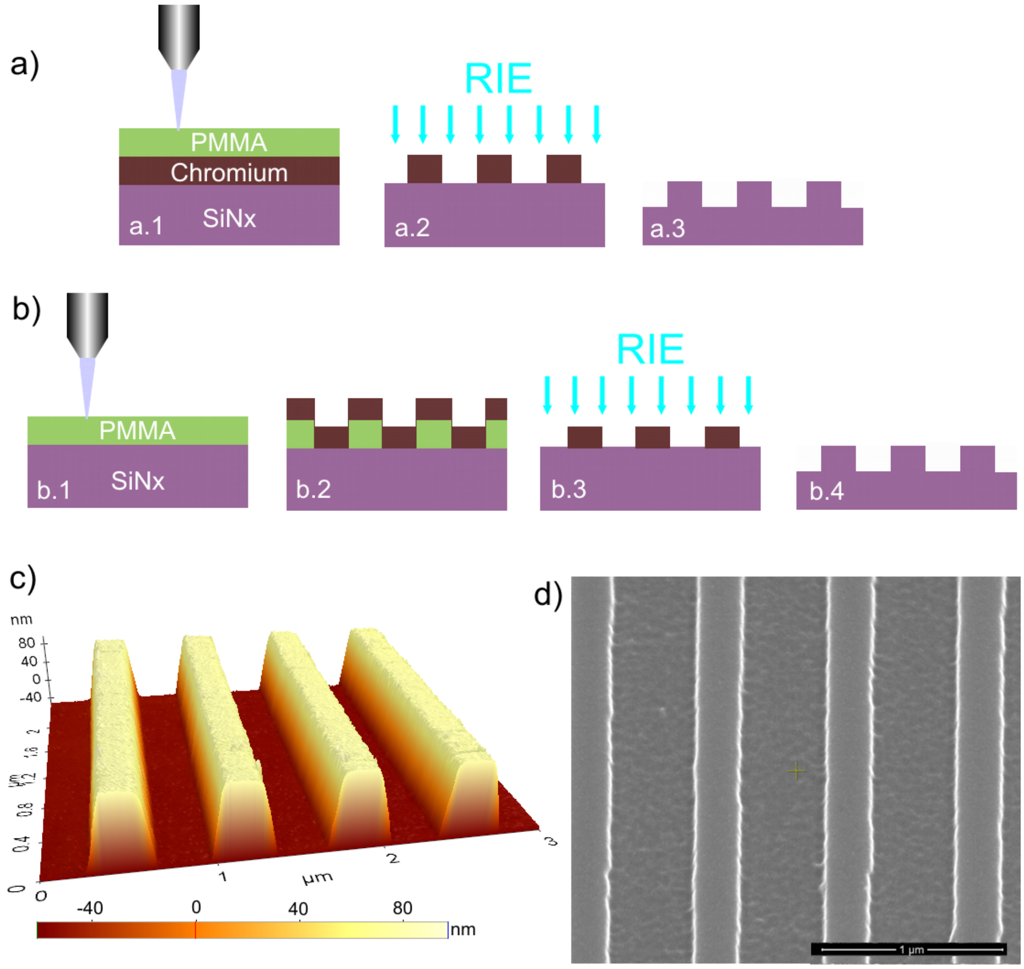

Figure 3.21: Fabrication steps of lamellar SiNx gratings. (a) Chromium etch process. (a.1) 740 nm period linear gratings are defined by electron beam exposure. (a.2) PMMA is developed and chromium is wet etched in diluted Cr etchant. SiNx is dry etched by RIE CHF_3:O_2 plasma. (a.3) Chromium mask is removed. (b) Chromium lift-off process. (b.1) Similar to (a.1) except there is no Cr layer initially. (b.2) Chromium sputtered on PMMA mask and lifted-off. (b.3-4) Same as the (a.2-3) (c) AFM topography image of lamellar SiNx gratings. (d) SEM image of lamellar SiNx gratings with thin Au/Pd coating.

3.2.3 Optical Lithography

Lamellar gratings with periods of Λ=3μm are fabricated using optical lithography (Fig.3.22). A positive photosensitive polymer (AZ5214) is spin-coated at 5000 rpm on the PECVD growth SiNx layer and pre-baked at 110 ^{o}C for 50 secs. UV light is exposed through a UV and visible-transparent mask (like quartz or glass) having opaque chromium grating patterns. Exposed regions are developed in 1:4 AZ400K:DI for 30 secs. Photoresist etch mask is then post-baked at 120 ^{o}C for 2 minutes for good stiction during the wet etch process. SiNx is wet etched in diluted HF and the remaining photoresist is removed by applying acetone and isopropanol.

In the case of lamellar grating fabrication, optical lithography duration is substantially shorter than electron beam lithography duration of the same size pattern. However, minimum feature size achievable using optical lithography is inherently limited by the diffraction of the light and is practically about sub-microns. Hence, only groove periods on the order of micrometers can be defined using this lithographic technique. Micron period gratings are appropriate for the excitation of surface plasmons at IR wavelengths.

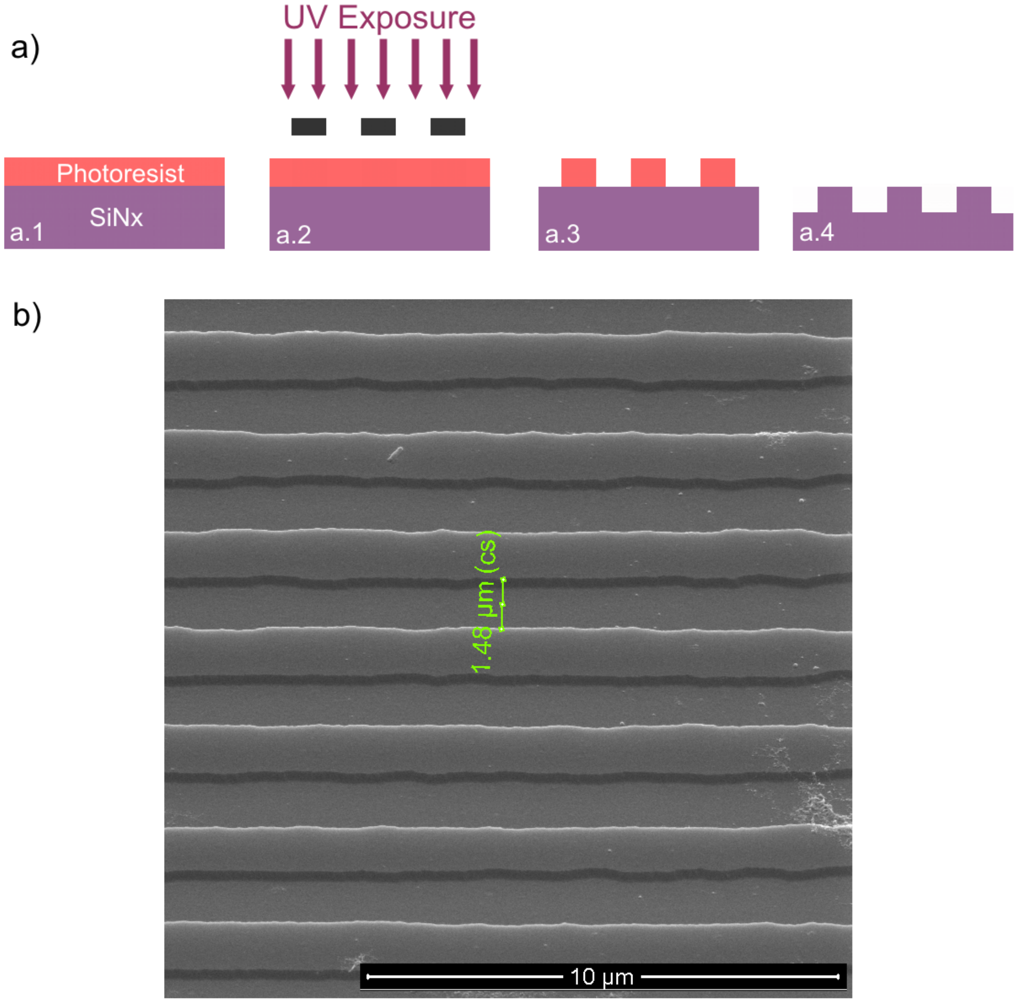

Figure 3.22: Fabrication steps of 3 µm period lamellar SiNx gratings using optical lithography. (a.1) A positive photosensitive polymer on the PECVD growth SiNx layer and pre-baked . (a.2) UV light is exposed through a grating mask. (a.3) Exposed regions are developed and photoresist mask is post-baked. (a.4) SiNx is wet etched in diluted HF and the remaining photoresist is removed by applying acetone and isopropanol. (b) Scanning electron micrograph of 3 µm period lamellar SiNx gratings

3.3 Characterization of Gratings

Topographic and plasmonic properties of silver coated gratings are characterized using atomic force microscopy and variable angle spectroscopic ellipsometry (V-VASE, J.A. Woollam), respectively. AFM topography images reveal the exact profile of silver coated gratings (Fig.3.24). A representative line profile which is averaged over a wide area is imported to RCWA simulation as the real grating profile while generating the numerical dispersion diagram. Experimental dispersion diagram is obtained by measuring the p-polarized reflected intensity with respect to both excitation wavelength and angle of incidence. Numerical and experimental results are observed to be in good agreement (Fig.3.25). θ_{FWHM}'s below 1 deg is achieved as estimated by the numerical analysis.

Spectroscopic scan measurement of another silver coated grating is also provided to show the polarization dependence of the SPP excitation in the grating coupling scheme. In the spectroscopic scan, Ψ and Δ are measured which are given by,

$$\frac{r_p}{r_s} = \tan(\Psi)e^{i\Delta}$$

where r_p and r_s are the normalized amplitudes of *s* and *p* components of the reflected light. Since surface plasmons are excited by only p components, Ψ diminishes and Δ shifts by 90 degrees at the resonance angles (Fig.3.26).

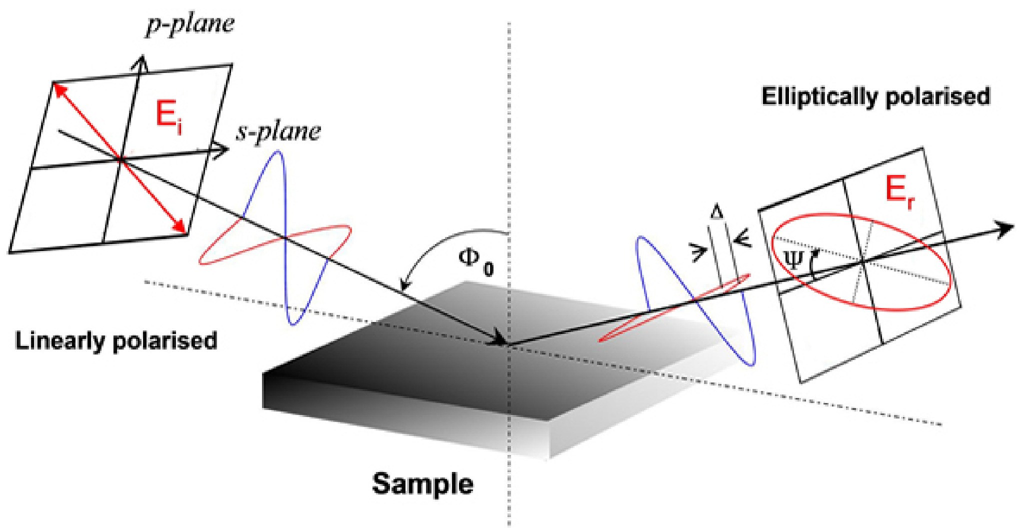

Figure 3.23: Elliptically polarization of the linearly polarized beam upon reflection

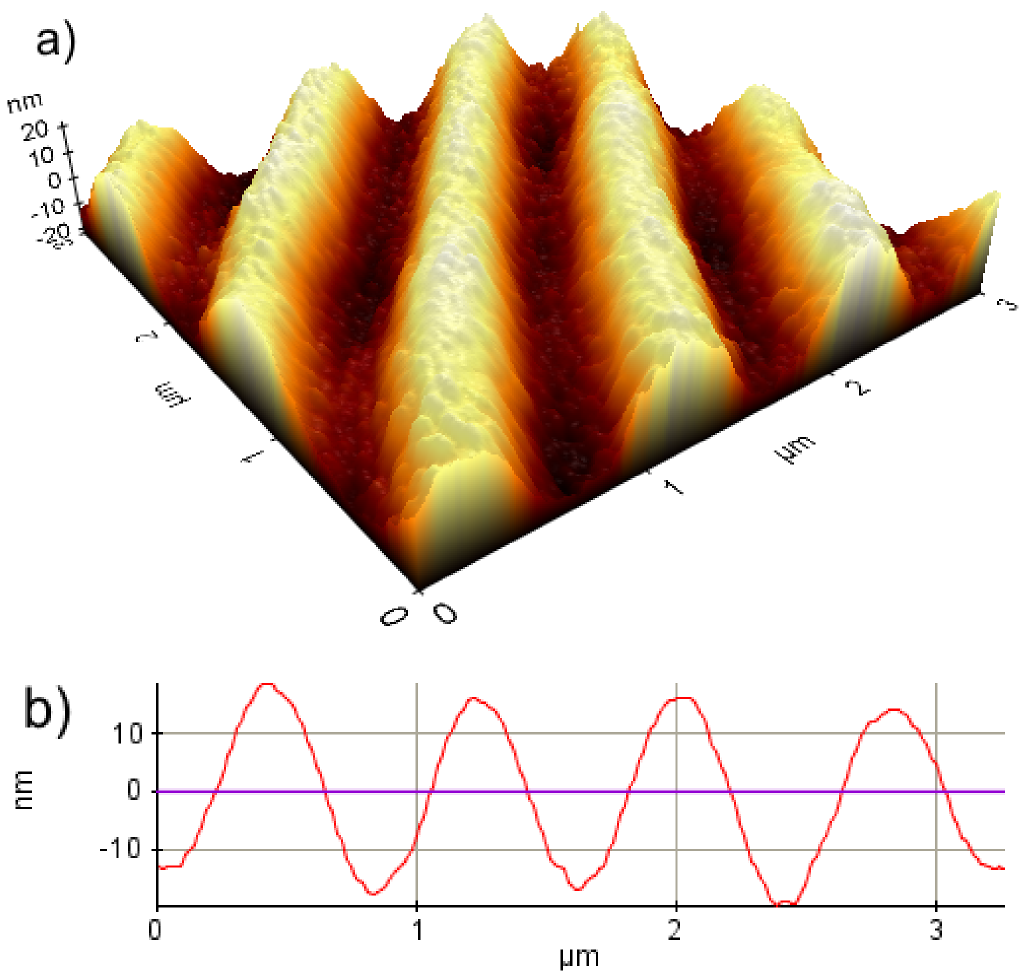

Figure 3.24: Topographic characterization of a silver coated grating. (a) AFM topography image. (b) A representative line profile.

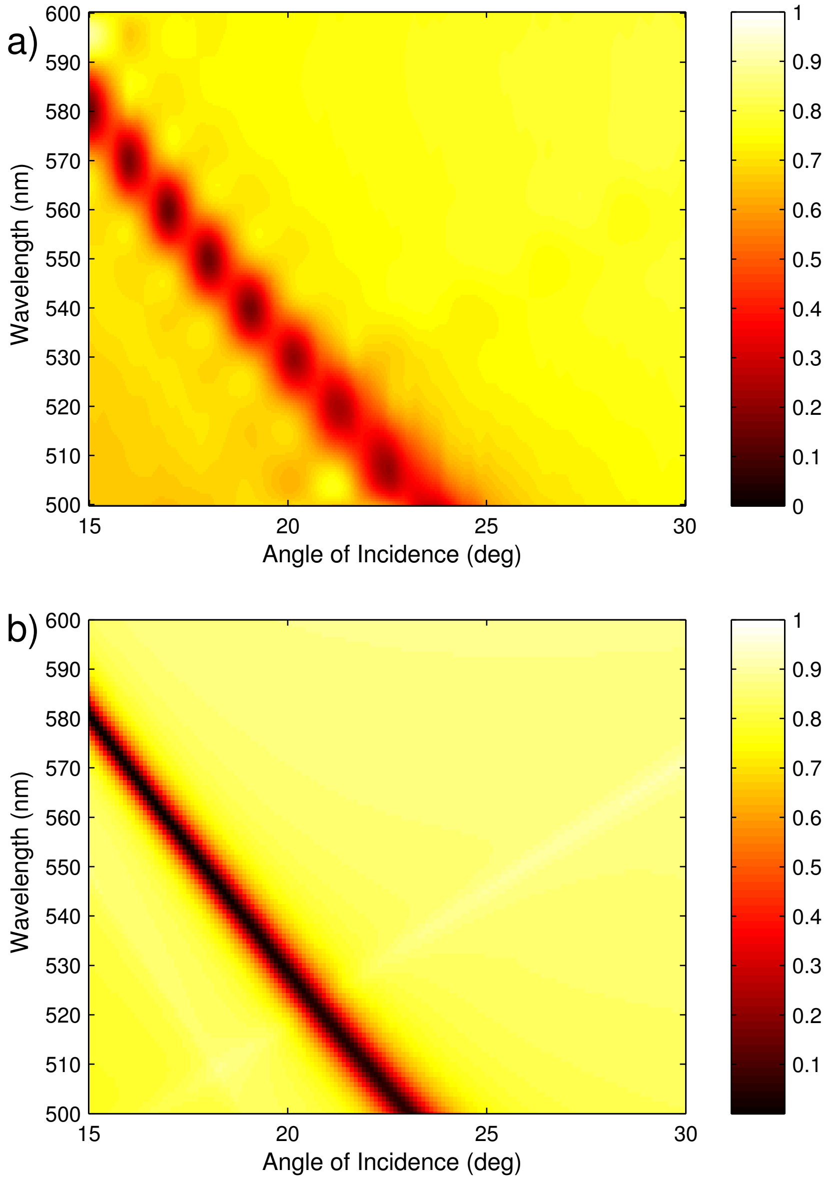

Figure 3.25: Plasmonic characterization of a silver coated grating (same as given in Fig.3.24). (a) Experimental dispersion curves (interpolated). (b) Numerical dispersion curves.

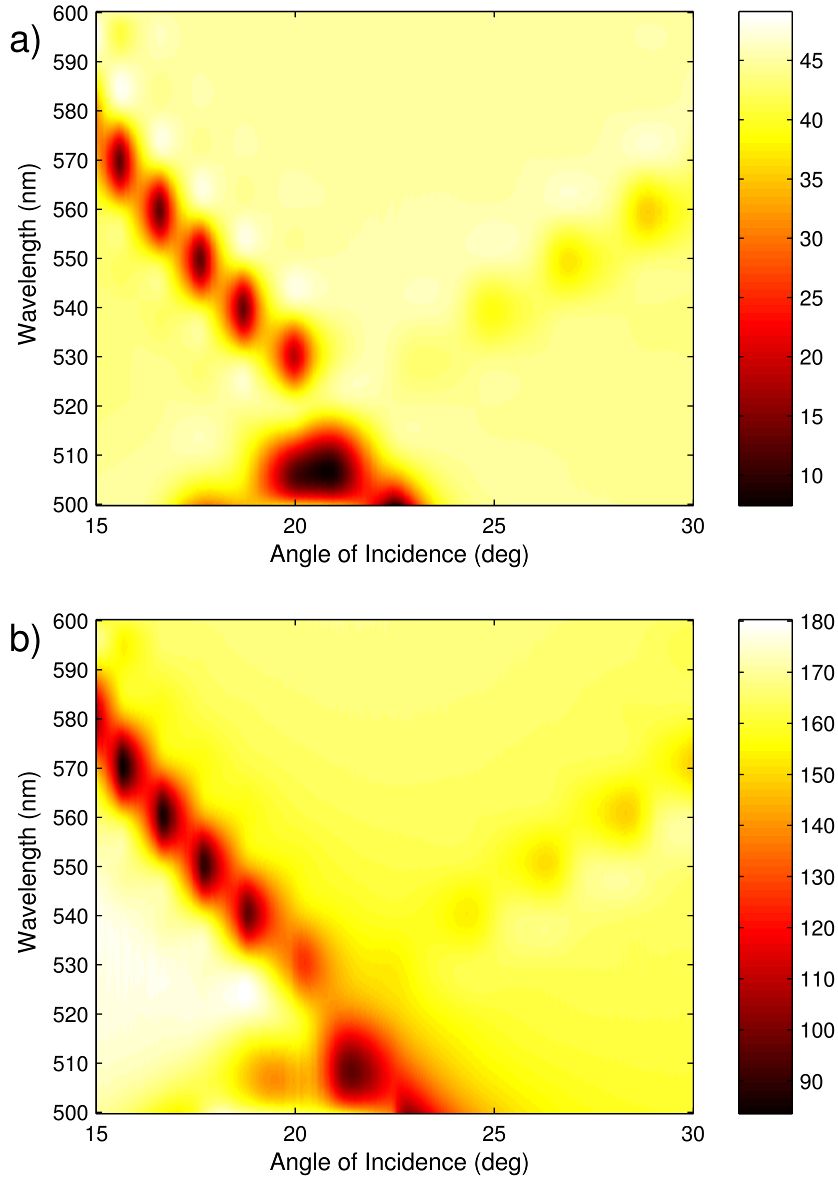

Figure 3.26: Spectroscopic scan measurements of a silver coated grating. (interpolated) (a) ψ with respect to the wavelength and the angle of incidence. (b) Δ with respect to the wavelength and the angle of incidence.

Chapter 4

Angular Displacement Detection Method

A new angular displacement detection method based on surface plasmon resonance is proposed. Two alternative designs are investigated as illustrated in Fig.4.1. Excitation light is incident at a bias angle maximizing the signal-to-noise ratio. Reflected or transmitted beam intensities are detected by a photodetector in single or double grating designs, respectively. Resonant transmission of light through the double grating structure is recently discussed. [27] Angular displacement is detected through the photocurrent change depending on the intensity change associated with the plasmonic excitation.

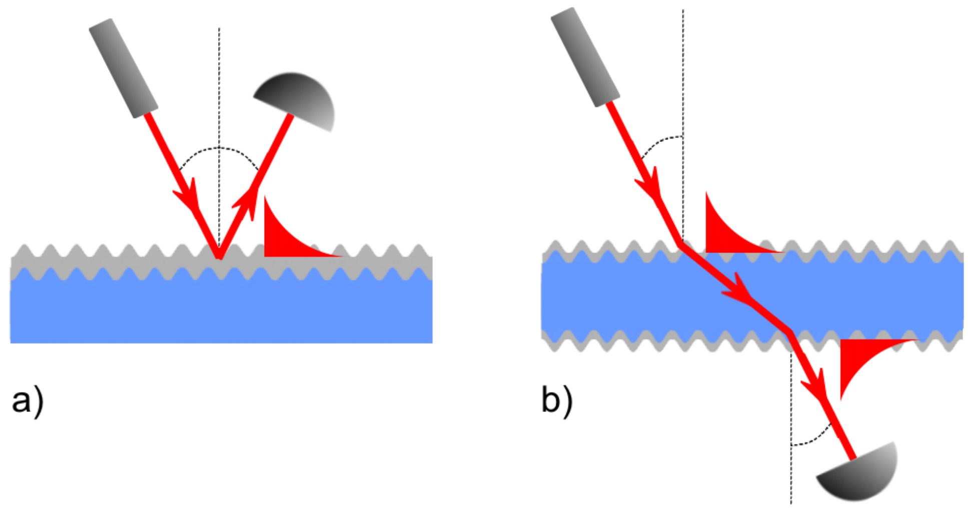

Figure 4.1: Illustration of the surface plasmon resonance based angular displacement detection schemes. (a) Single grating with thick metallization to read the reflected beam intensity at the same side with the light source. (b) Double grating with thin metallization to read the transmitted intensity at the opposite side of the light source

The photodetector current is given by $i_{pd} = P\Re$ where P is the power of the incident beam upon the photodetector and $\Re$ is the spectral responsivity of the photodetector. The spectral responsivity is given by $\Re = \frac{\eta q \lambda}{hc}$ where η is the quantum efficiency, q is the charge for one electron, λ is the wavelength, h is the

Planck's constant and c is the speed of light. For a silicon pin photodiode, $\Re \approx 0.41$ A/W for λ =633 nm and $\Re \approx 0.69$ A/W for λ =950 nm assuming that the quantum efficiency is $\eta = 0.9$. Photon shot noise current which arises due to the random arrivals of the photons to the photodiode is expressed as $\sqrt{\langle i_{sh}^2 \rangle} = \sqrt{2qi_{pd}B}$ where B is the measurement bandwidth in hertz. Shot noise equivalent angular displacement (SNEAD) may be considered as the minimum detectable angular displacement for our detection scheme as like other optical detection schemes. The angular sensitivity is defined as $S = \frac{\partial i_{pd}}{\partial \theta}$ where θ is the angle of incidence. SNEAD is evidently found as

$$\sqrt{\langle \theta_{sh}^2 \rangle} = \frac{\sqrt{\langle i_{sh}^2 \rangle}}{\left(\frac{\partial i_{pd}}{\partial \theta}\right)} \tag{4.1}$$

Intensity of the incident beam as a function of the angle of incidence is numerically calculated using RCWA (Fig.4.2). As a first order approach, the photodetector current as a function of the angle of incidence ignoring the spectral width, $\Delta\lambda$ and beam divergence, β of the light source, is expressed as

$$i_{pd}(\theta) = P(\theta, \lambda_e)\Re(\lambda_e) \tag{4.2}$$

where λ_e is the SPP excitation wavelength of the incident beam. Figure 4.3 shows calculated SNEAD as a function of the excitation wavelength for a silicon pin photodiode. Nanoradian per root hertz SNEAD is found to be achievable for a 1mW light source.

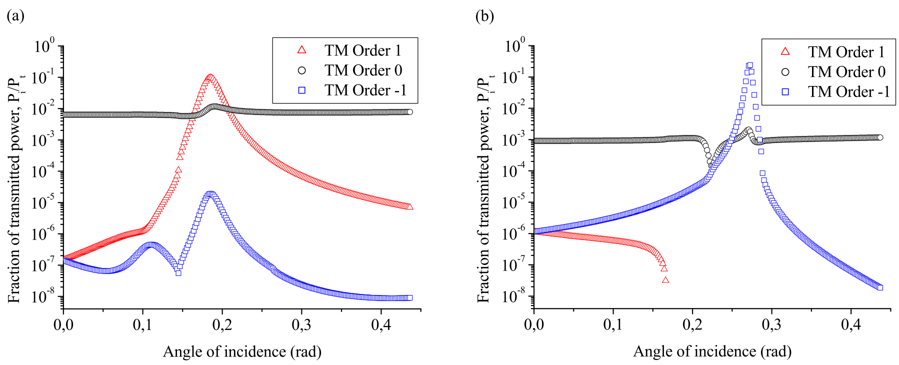

Figure 4.2: Fraction of transmitted powers, Pi/Pt with respect to the angle of incidence for TM beams with excitation wavelengths of λ_e=633 nm (a), and (b) λ_e=950 nm.

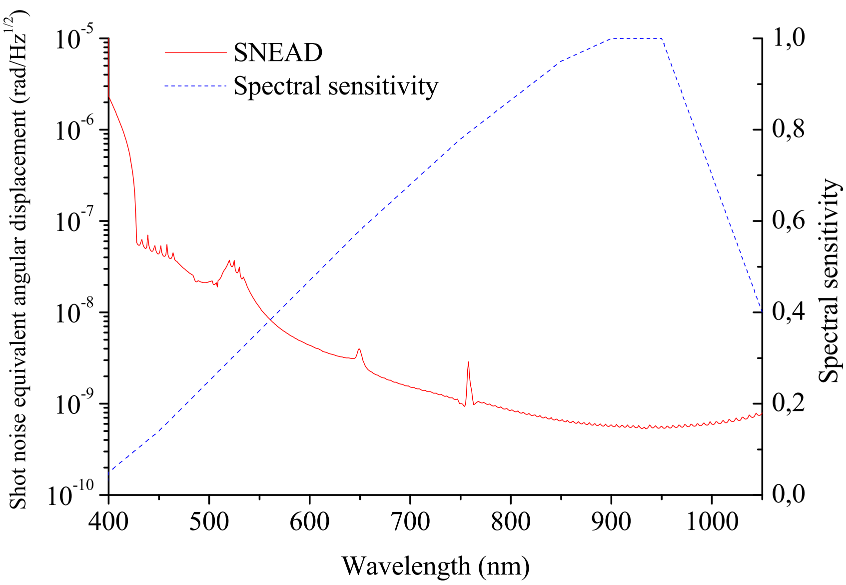

Figure 4.3: Shot noise equivalent angular displacement with respect to the excitation wavelength of the incident beam for a commercial silicon PIN photodiode having the plotted spectral sensitivity

In a more realistic case with light sources having non-zero spectral widths, the photodetector current is approximated by

$$i_{pd}(\theta) \approx \int_{\lambda_{min}}^{\lambda_{max}} P(\theta,\lambda)\Re(\lambda)d\lambda \qquad (4.3)$$

Figure 4.4.a shows calculated SNEAD as a function of the angle of incidence for various selected spectral widths. SNEAD rises up by 2 orders of magnitude as $\Delta\lambda$ is increased from 5 nm to 80 nm.

In another realistic case with light sources having non-zero beam divergence angles, the photodetector current is approximated by

$$i_{pd}(\theta) \approx \Re(\lambda_e) \int_{\alpha_{min}}^{\alpha_{max}} P(\theta-\alpha,\lambda_e)d\alpha \qquad (4.4)$$

Figure 4.4.b shows calculated SNEAD as a function of the angle of incidence for various selected beam divergence angles. 3 orders of magnitude increase in SNEAD is observed as β is expanded from 3 mrad to 300 mrad.

(a)

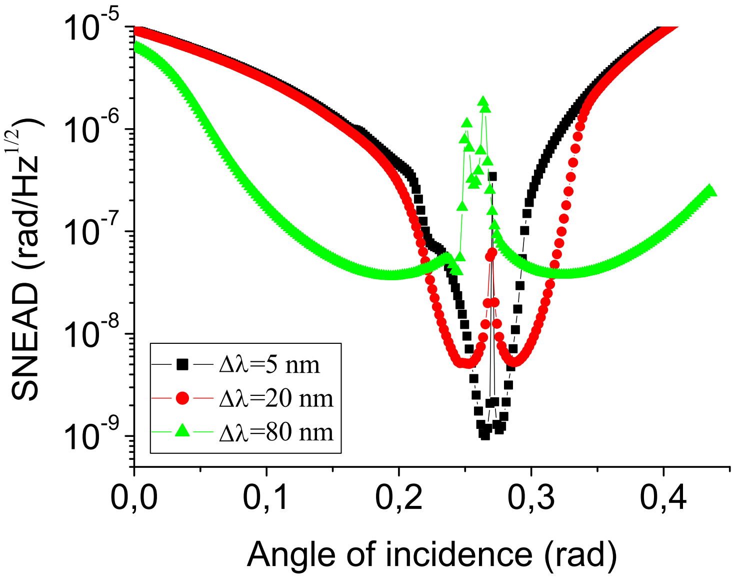

(b)

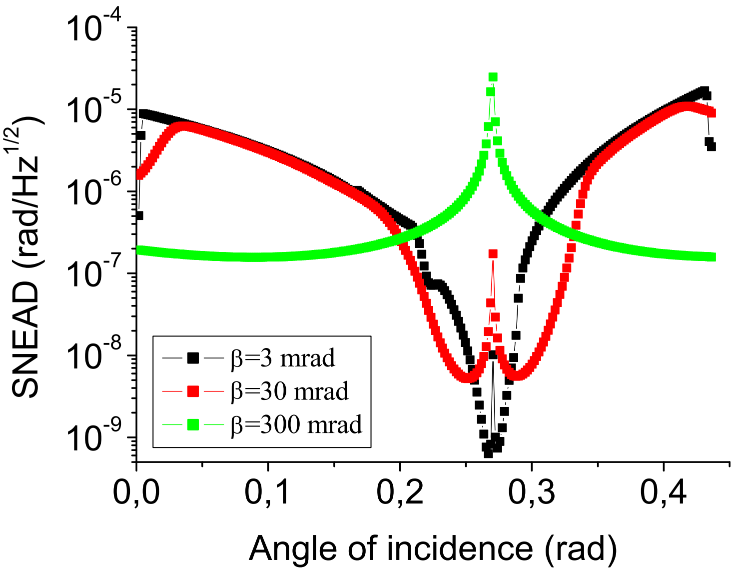

Figure 4.4: Shot noise equivalent angular displacements with respect to the angle of incidence for realistic cases. (a) For various spectral widths. (b) For various beam divergence angles.

Chapter 5

Design, Fabrication and Characterization of MEMS Devices

5.1 Theoretical Background

5.1.1 Beam Theory

The dynamic behavior of beam resonators can be analyzed by Euler-Bernoulli theory.[28] The force balance on the infinitesimal section of an undamped beam is expressed as

$$\frac{\partial^2}{\partial y^2} EI \frac{\partial^2 U(y,t)}{\partial y^2} + \rho A \frac{\partial^2 U(y,t)}{\partial t^2} = F(y,t) \tag{5.1}$$

where E is the Young's modulus, I is the moment of inertia, ρ is the mass density, A is the cross-sectional area of the beam and $F(y,t)$ is the time-varying external load in the z-direction. In Figure 5.1, a doubly clamped beam loaded by $F(y,t)$ at its fundamental mode is schematically depicted.

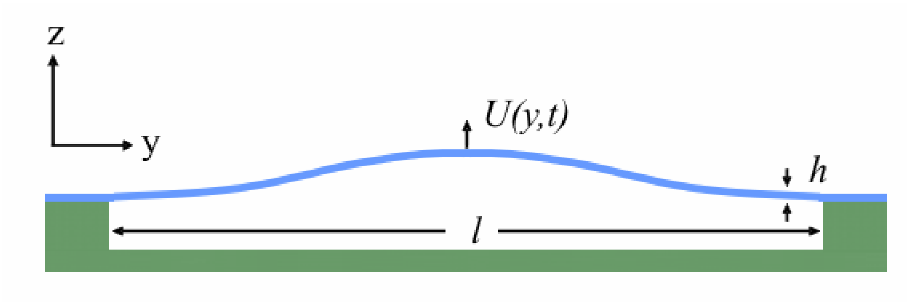

Figure 5.1: Fundamental mode shape of a doubly clamped beam resonator with length l, thickness h and width w. $U(y,t)$ is the position and time dependent displacement of the beam in the z-direction .

For a beam of rectangular cross-section with thickness h and width w, the cross-sectional area is $A = hw$ and the moment of inertia is $I = \frac{1}{12} h^3 w$.

$\frac{\partial^2}{\partial y^2} EI \frac{\partial^2 U(y,t)}{\partial y^2}$ term represents the stress formation due to the deformation and $\rho A \frac{\partial^2 U(y,t)}{\partial t^2}$ comes from the inertial effect of the motion. The displacement $U(y,t)$ can be separated into the time and position dependent components in the form of summation of modes as,

$$U(y,t) = \sum_n q_n(t)\varphi_n(y) \tag{5.2}$$

where n is the mode number, $\varphi_n(y)$ is the position dependent mode shape function and $q_n(t)$ is the time dependent amplitude of motion. Assuming that the beam is isotropic and has a uniform cross-section, Eq.5.2 is substituted into Eq.5.1 as,

$$EI\sum_n q_n(t)\frac{\partial^2}{\partial y^2}\frac{\partial^2 \varphi_n(y)}{\partial y^2} + \rho A \sum_n \varphi_n(y)\frac{\partial^2 q_n(t)}{\partial t^2} = F(y,t) \tag{5.3}$$

For the homogenous case of $F(y,t) = 0$,

$$\frac{EI}{\rho A \varphi_n(y)}\frac{\partial^2}{\partial y^2}\frac{\partial^2 \varphi_n(y)}{\partial y^2} = -\frac{1}{q_n(t)}\frac{\partial^2 q_n(t)}{\partial t^2} = \omega_n^2 \tag{5.4}$$

for each mode n. The first part of the equation can be formulated as

$$\begin{aligned} &\frac{\partial^4 \varphi_n(y)}{\partial y^4} - \alpha_n^4 \varphi_n(y) = 0, \\ &\alpha_n = \left(\frac{\rho A}{EI}\right)^{1/4} \omega_n^{1/2} \end{aligned} \tag{5.5}$$

where α_n is a constant depending on the geometry and material of the beam for each mode n. Eq.5.4 has a solution of the form

$$\varphi_n(y) = a_n \cos(\alpha_n y) + b_n \sin(\alpha_n y) + c_n \cosh(\alpha_n y) + d_n \sinh(\alpha_n y) \tag{5.6}$$

For a doubly clamped beam, the boundary conditions can be expressed as

$$\varphi_n(0) = \varphi_n(l) = \left.\frac{d\varphi_n}{dy}\right|_{y=0} = \left.\frac{d\varphi_n}{dy}\right|_{y=l} = 0 \tag{5.7}$$

Applying these conditions on Eq.5.6 yields

$$\begin{aligned}
&\varphi_n(y) = a_n\left[\cosh(\alpha_n y) - \cos(\alpha_n y)\right] + b_n\left[\sin(\alpha_n y) - \sinh(\alpha_n y)\right], \\
&\frac{a_n}{b_n} = \frac{\left[\cosh(\alpha_n l) - \cos(\alpha_n l)\right]}{\left[\sin(\alpha_n l) - \sinh(\alpha_n l)\right]}, \\
&\cos(\alpha_n l)\cosh(\alpha_n l) - 1 = 0
\end{aligned} \tag{5.8}$$

Non-trivial α_n and $\frac{a_n}{b_n}$ values are numerically calculated and shown in Table 5.1.[29] Figure 5.2 shows the first four mode shapes of a doubly clamped beam.

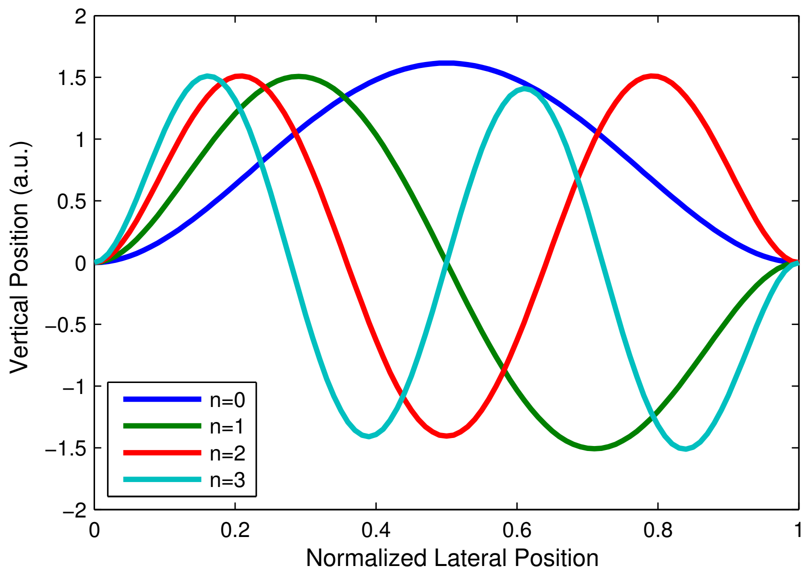

Figure 5.2: The first four mode shapes of a doubly clamped beam

For a cantilever beam, the boundary conditions become

$$\varphi_n(0) = \left.\frac{d\varphi_n}{dy}\right|_{y=0} = \left.\frac{d^2\varphi_n}{dy^2}\right|_{y=l} = \left.\frac{d^3\varphi_n}{dy^3}\right|_{y=l} = 0 \tag{5.9}$$

Eq.5.6 is solved in the same manner for the cantilever beam and the constants are numerically extracted. Using Eq.5.5, the resonance frequency of each mode is then found by

$$\omega_n = \alpha_n^2\sqrt{\left(\frac{EI}{\rho A}\right)} \tag{5.10}$$

Table 5.1: Modal parameters for the first four modes of a doubly-clamped and cantilever beam

n	0	1	2	3
$\alpha_n l$ (doubly clamped)	4.730	7.853	10.996	14.137
$\alpha_n l$ (cantilever)	1.875	4.694	7.5	10.996

The displacement of the device at a certain position y_n and at a limited mode n is expressed from Eq.5.2 as

$$u(t) = U(y_n, t) = q_n(t)\varphi_n(y) \tag{5.11}$$

At the fundamental mode, maximum deformed positions of the doubly clamped and cantilever beams are taken as $y_0 = \frac{l}{2}$ and $y_0 = l$, respectively. Effective constants are found as

$$\begin{aligned} \frac{\omega_0}{2\pi} &= 1.03\frac{h}{l^2}\sqrt{\frac{E}{\rho}}, \\ m &= 0.76\rho hwl, \\ k &= 32\frac{Eh^3w}{l^3} \end{aligned} \tag{5.12}$$

for the doubly clamped beam, and

$$\begin{aligned} \frac{\omega_0}{2\pi} &= 0.16\frac{h}{l^2}\sqrt{\frac{E}{\rho}}, \\ m &= 0.24\rho hwl \\ k &= \frac{1}{4}\frac{Eh^3w}{l^3} \end{aligned} \tag{5.13}$$

for the cantilever beam.

5.1.2 Fundamental Limit of Displacement Measurements

A beam resonator can be modeled as a damped harmonic oscillator with lumped parameters extracted from Euler-Bernoulli beam theory. The out-of-plane motion is formulated as

$$m\ddot{x} + b\dot{x} + kx = F(t) \tag{5.14}$$

where m is the effective mass, b is the damping coefficient, k is the spring constant and $F(t)$ is the applied force. Hence, force-to-displacement transfer function is

$$H(s) = \frac{x(s)}{F(s)} = \frac{1}{m}\frac{1}{s^2 + \frac{b}{m}s + \frac{k}{m}} \tag{5.15}$$

In terms of the natural angular frequency, ω_0 and the quality factor , Q, the transfer function in the frequency domain is expressed as

$$H(j\omega) = \frac{1}{m}\frac{1}{\omega_0^2 - \omega^2 + j\frac{\omega\omega_0}{Q}} \tag{5.16}$$

where $\omega_0 = \sqrt{\frac{k}{m}}$ and $Q = \frac{m\omega_0}{b}$. Having found $H(j\omega)$, the power spectral density of the displacement is found as

$$S_x(\omega) = \frac{1}{m^2}\frac{S_F(\omega)}{(\omega_0^2 - \omega^2)^2 + (\frac{\omega\omega_0}{Q})^2} \tag{5.17}$$

from

$$S_x(\omega) = \left|H(jw)\right|^2 S_F(\omega) \tag{5.18}$$

where $S_F(\omega)$ is the power spectral density of the applied force.

The fundamental limit of displacement measurements is imposed by the thermal-mechanical noise. Thermal-mechanical noise originates from the random motion of the mechanical device driven by the thermal noise as a consequence of the fluctuation-dissipation theorem. The mean square displacement $\left\langle x_{th}^2 \right\rangle$ associated with the thermal-mechanical noise satisfy

$$\frac{1}{2}k\left\langle x_{th}^{2}\right\rangle = \frac{1}{2}k_{B}T \tag{5.19}$$

where k_B is Boltzmann's constant and T is the temperature of the system. The power spectral density of the thermal-mechanical force noise is considered to have a white spectrum over a wide range of frequencies ($\omega \ll k_B T/\hbar$) and given by

$$S_{F_{th}}(\omega) = \frac{4kk_B T}{\omega_0 Q} \tag{5.20}$$

The power spectral density of the thermal-mechanical displacement fluctuations is then found as

$$S_{x_{th}}(\omega) = \frac{4kk_B T}{m^2\omega_0 Q}\frac{1}{(\omega_0^2-\omega^2)^2+(\frac{\omega\omega_0}{Q})^2} \tag{5.21}$$

The root mean square displacement within a bandwidth B at $\omega \ll \omega_0$ is found as

$$\sqrt{\left\langle x_{th}^{2}\right\rangle_B} = \sqrt{\frac{4k_B TB}{k\omega_0 Q}} \tag{5.22}$$

This is considered as the fundamental limit of a displacement measurement.

5.2 Design and Fabrication of MEMS Devices

5.2.1 Design of MEMS Devices

MEMS displacement sensor designs relying on the principle of angular displacement detection scheme are proposed. Surface plasmon resonance grating structures are transferred on conventional micromembranes. As schematically illustrated in Fig.5.3, two types of such particular designed micromembranes are introduced: corrugated microcantilevers (singly clamped) and corrugated microbridges (doubly clamped). Mechanical attributes of devices derived from Euler-Bernoulli beam theory are calculated as given in Table. 5.2. Flexural mode shapes at the fundamental mode of devices are numerically simulated using finite element analysis as shown in Fig.5.4.

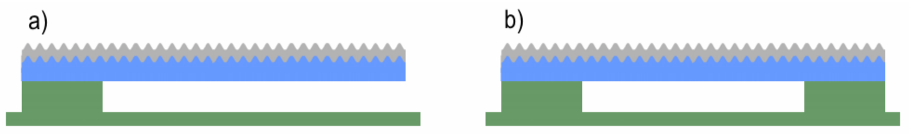

Figure 5.3: Schematic illustration of corrugated micromembranes.(a) Corrugated microcantilever (singly clamped). (b) Corrugated microbridge (doubly clamped).

Table 5.2: Mechanical attributes of micromembranes. Shallow corrugation and thin metallization are not included in the calculations. For PECVD grown SiNx film, Young's modulus, E is taken as 100 GPa and mass density, ρ is taken 3170 kg/m^3.

	$w \times h \times l$ (μm)	f_0 (kHz)	k (N/m)	m (ng)
Microcantilever	45 x 0.8 x 150	31.95	0.17	4.1
Microbridge	150 x 0.8 x 700	26.05	0.72	202

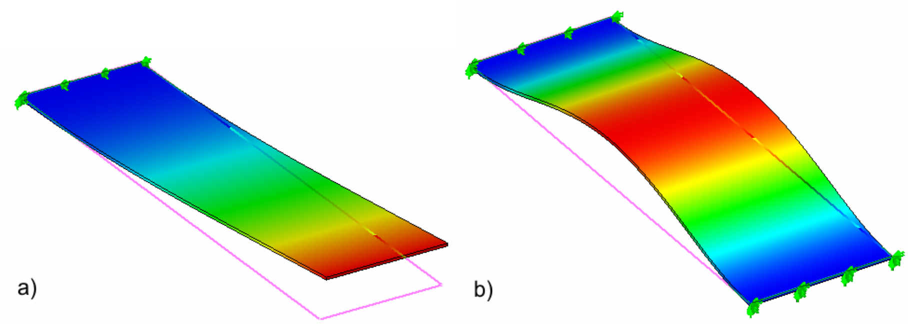

Figure 5.4: Fundamental flexural mode shapes simulated using finite element analysis. (a) Microcantilever. (b) Microbridge.

In these devices, out-of-plane displacement is interpreted as angular displacement depending on the membrane coordinate where the excitation light is incident upon. For the corrugated microcantilever design, maximum deflection occurs at the free end at the fundamental mode. Angular displacement $\Delta\theta$ of the free end with respect to the membrane axis is approximated as

$$\Delta\theta = \frac{\Delta x}{l} \tag{5.23}$$

where l is the length of the cantilever and Δx is the out-of-plane displacement. $\Delta\theta$ is measured using the angular displacement detection scheme. From Eq.5.22, the fundamental limit of the angular displacement measurement is expressed as

$$\sqrt{\left\langle \theta_{th}^2 \right\rangle_B} = \frac{1}{l}\sqrt{\frac{4k_B TB}{k\omega_0 Q}} \tag{5.24}$$

Including the shot noise equivalent angular displacement $\sqrt{\left\langle \theta_{sh}^2 \right\rangle_B}$ that originates from the angular displacement detection scheme, the minimum detectable angular displacement (MDAD) can be expressed as

$$\sqrt{\left\langle \theta_{tot}^2 \right\rangle_B} = \sqrt{\left\langle \theta_{th}^2 \right\rangle_B + \left\langle \theta_{sh}^2 \right\rangle_B} \tag{5.25}$$

When the grating coupler characterized in Chapter 3.3 (Fig.3.24) is used in the angular displacement detection scheme, shot noise equivalent angular displacement becomes $\sqrt{\left\langle \theta_{sh}^2 \right\rangle_B} \approx 0.135$ nanodeg/$\sqrt{Hz}$ for a monochromatic (λ_e=633 nm) and collimated laser beam with 1mW optical power. For a corrugated microcantilever with length l=150 μm having the grating coupler in question, shot noise equivalent displacement corresponds to $\sqrt{\left\langle x_{sh}^2 \right\rangle_B} \approx 20$ fm/$\sqrt{Hz}$ whereas thermal-mechanical displacement noise is about $\sqrt{\left\langle x_{th}^2 \right\rangle_B} \approx 7$ fm/$\sqrt{Hz}$ for a quality factor of Q=10000 and at T=300K.

5.2.2 Fabrication of MEMS Devices

Corrugated micromembranes are fabricated using conventional micromachining techniques in addition to surface plasmon resonance grating fabrication procedures. (100) Silicon wafer is used as the substrate layer. SiNx is grown on silicon using plasma enhanced chemical vapor deposition (PECVD). SPR gratings are transferred to the SiNx layer following the processes explained in Chapter 3.2. Cantilever or bridge mask is defined on the corrugated SiNx layer using optical lithography (Fig.5.5). Membrane sides should be aligned as parallel to the {100} planes. Mask pattern is transferred to SiNx layer by dilute HF wet etching. Membranes are released by plane-selectively etching of silicon planes in 30% KOH solution at 85 ^{o}C. The {110} planes are etched in KOH about twice as rapidly as {100} planes, while {111} planes are etched at a rate about 100 times slower than for {100} planes.[30] Chromium is sputtered on the membranes for good stiction with the following metal coating. Silver or gold is coated by thermal evaporation. Optical microscope images of fabrication steps are shown in Figure 5.6. Scanning electron microscope images of devices are shown in Figure 5.7.

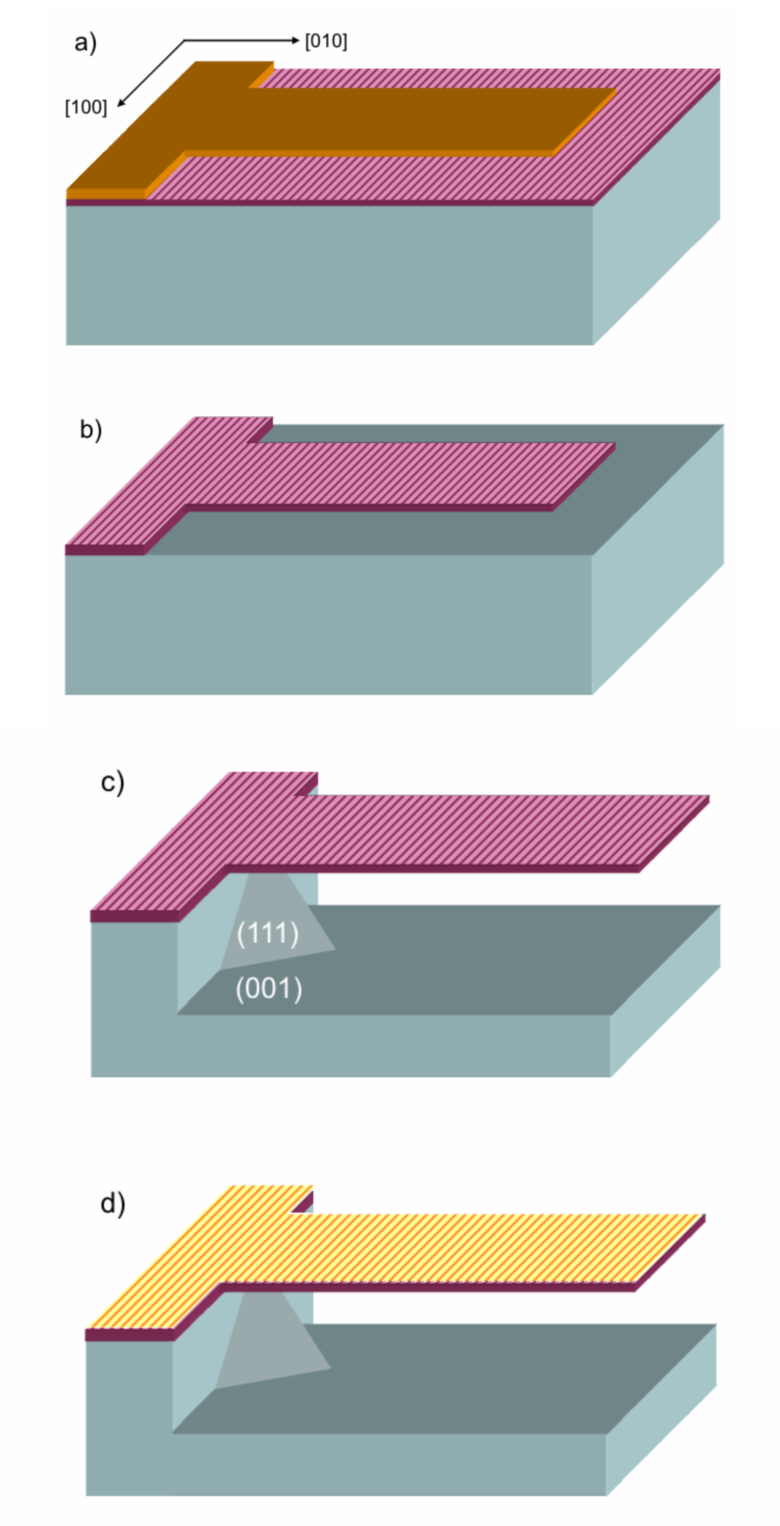

Figure 5.5: Fabrication steps of a corrugated microcantilever. (a) Cantilever mask is defined by optical lithography. (b) Corrugated SiNx layer is wet etched by dilute HF. (c) Silicon substrate is plane-selectively wet etched by KOH solution. (d) Metal (silver or gold) is coated using thermal evaporation.

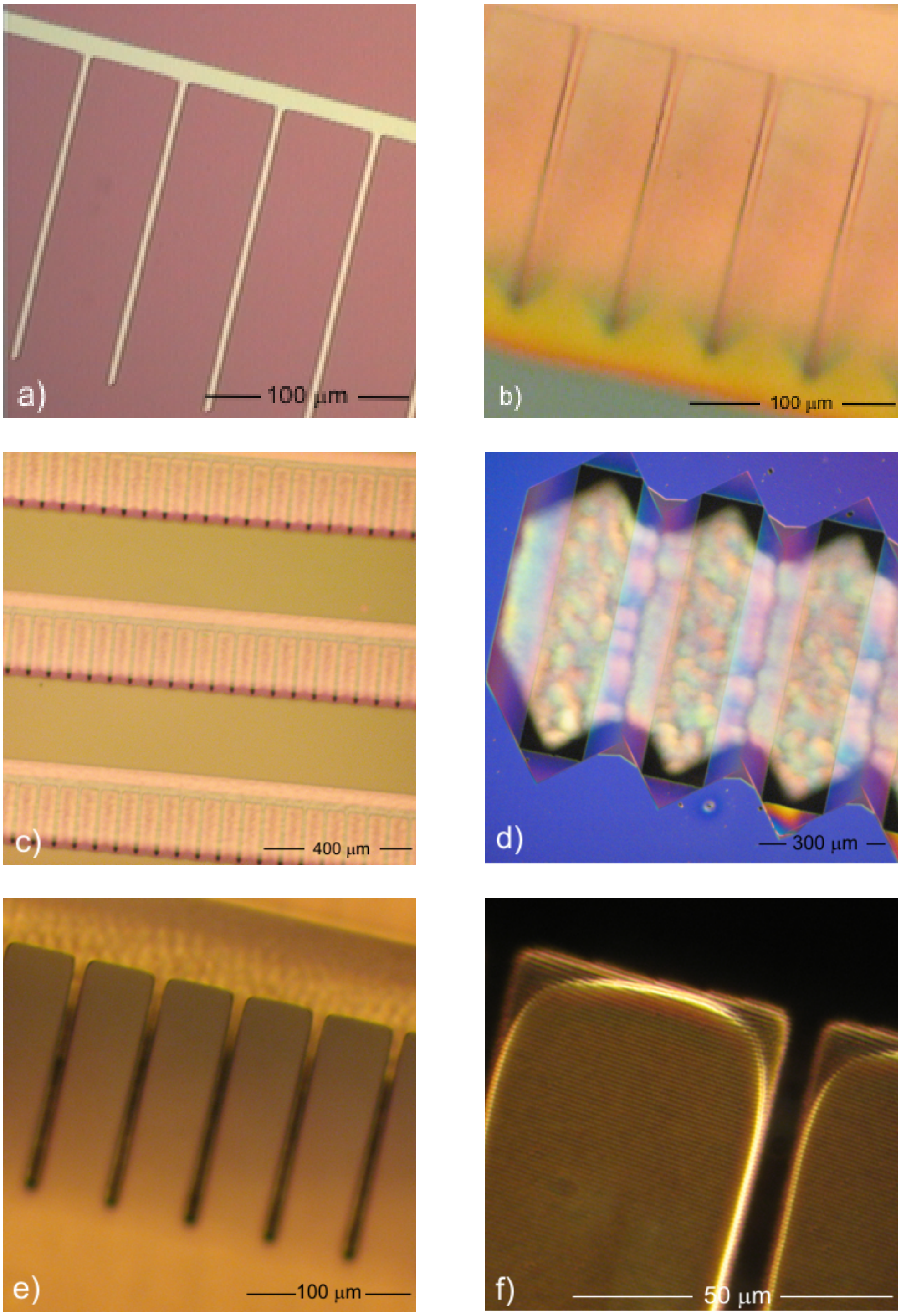

Figure 5.6: Optical microscope images of fabrication steps. (a) Cantilever pattern is transferred to SiNx layer. (b) SiNx microcantilevers are released. (c) Array view of released cantilevers. (d) Released microbridges. (e) After thin metallization. (f) Corrugations on a microcantilever

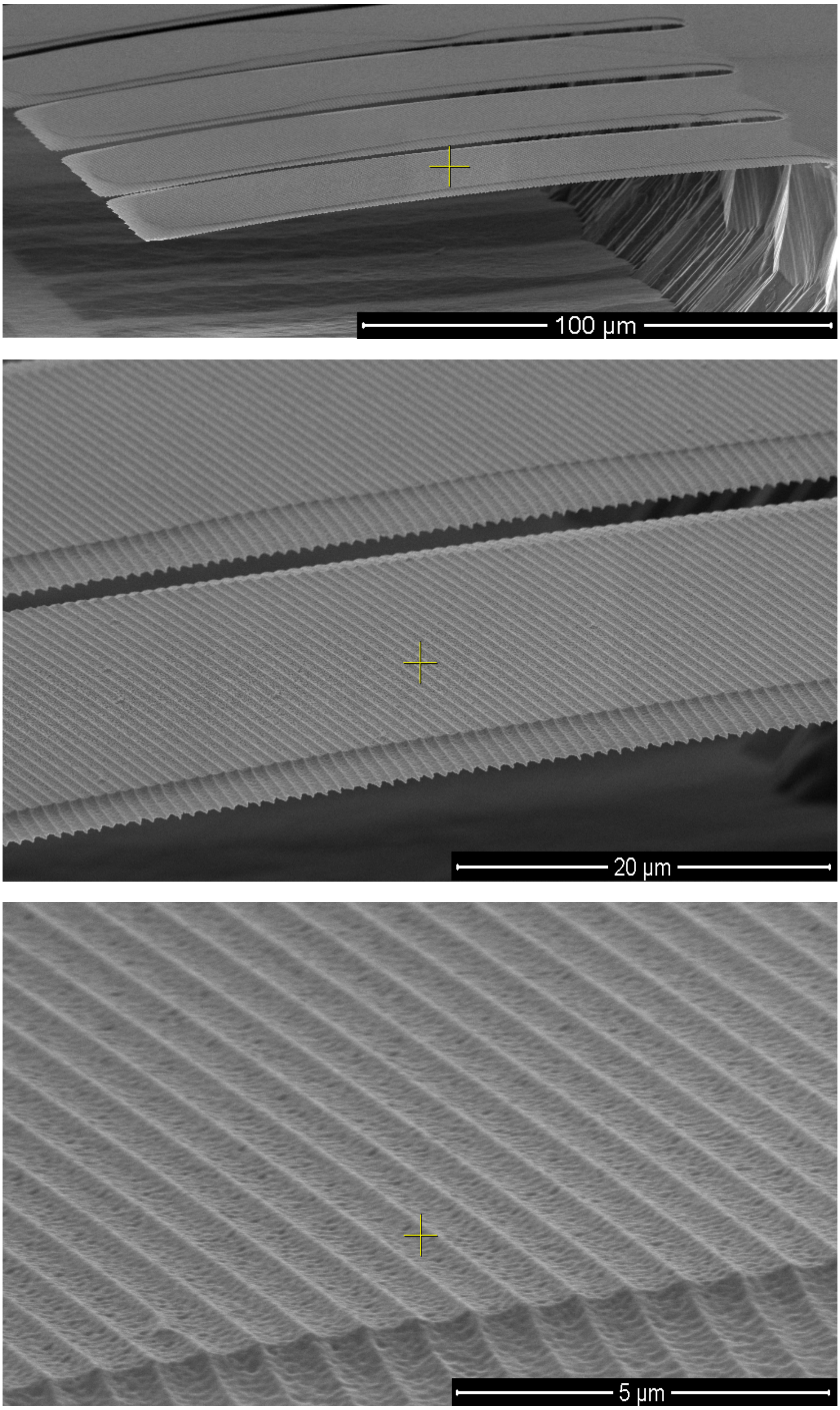

Figure 5.7: Scanning electron microscope images of corrugated microcantilevers

5.3 Characterization of MEMS Devices

5.3.1 Spectral Analysis Using Atomic Force Microscopy Setup

Frequency domain response of devices is analyzed using a commercial atomic force microscopy (MFP-30, Asylum Research) setup. AFM uses beam bounce method to measure the deflection of the cantilevers. In this method, a semiconductor diode laser beam is bounced off from the back side of the cantilever onto a position sensitive photodetector. This detector measures the bending of the cantilever. Here, corrugated microcantilever sample is mounted at the cantilever holder just like an AFM cantilever (Fig.5.8). Power spectral density of the photodetector response is plotted (Fig.5.9). Sharp peak at 30 KHz is due to the Brownian motion at the fundamental resonance frequency of the cantilever. This is consistent with the calculated fundamental resonance of a non-corrugated and non-metallized PECVD grown SiNx cantilever of the same sizes as 31.95 kHz.

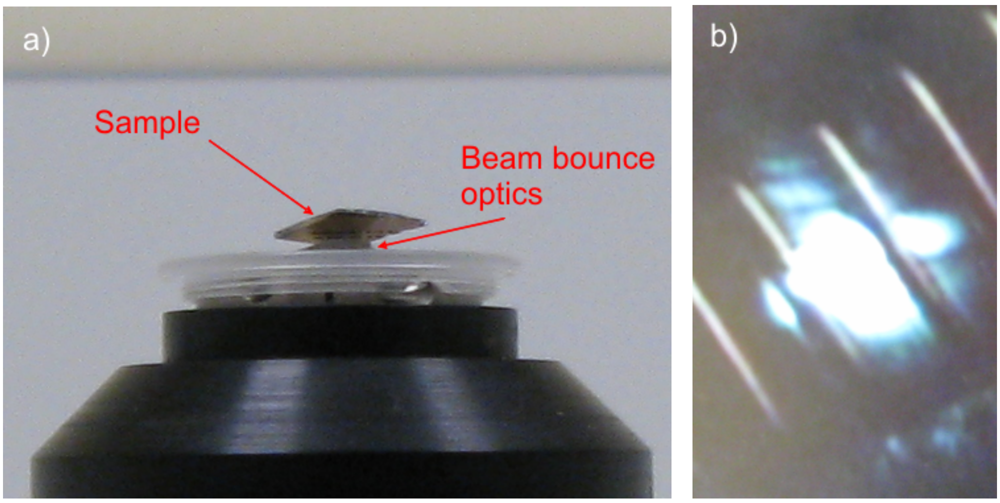

Figure 5.8: Use of AFM setup to measure the frequency response of a corrugated cantilever. (a) Sample is mounted at AFM cantilever holder. (b) CCD image of the laser pointed on the cantilever.

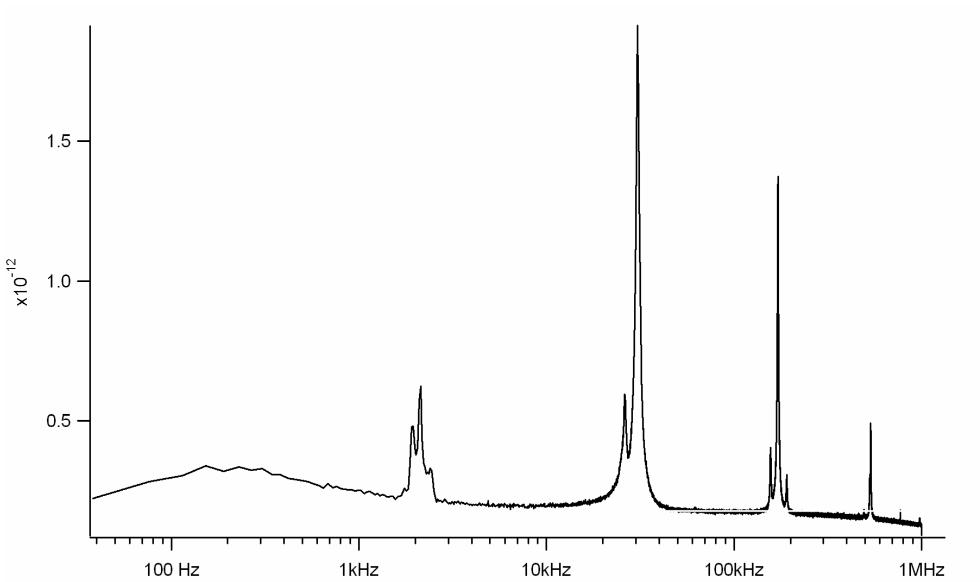

Figure 5.9: Power spectral density of the photodetector response. Sharp peak at 30 kHz is due to the Brownian motion at the fundamental resonance frequency of the cantilever.

5.3.2 Modal Analysis Using Scanning White Light Interferometry

Phase-dependent mode shapes of cantilevers are imaged using optical profilometer (Newview 7200, Zygo) based on scanning white light interferometry for the fundamental and second resonant modes (Fig.5.10 and Fig.5.11). Cantilevers are driven by a piezo electric transducer (AE0203D08F, Thorlabs) with a peak-to-peak amplitude of $V_{pp} = 5V$. Fundamental resonance frequency is measured to be 32.9 kHz. Second resonance frequency is measured as 210 kHz.

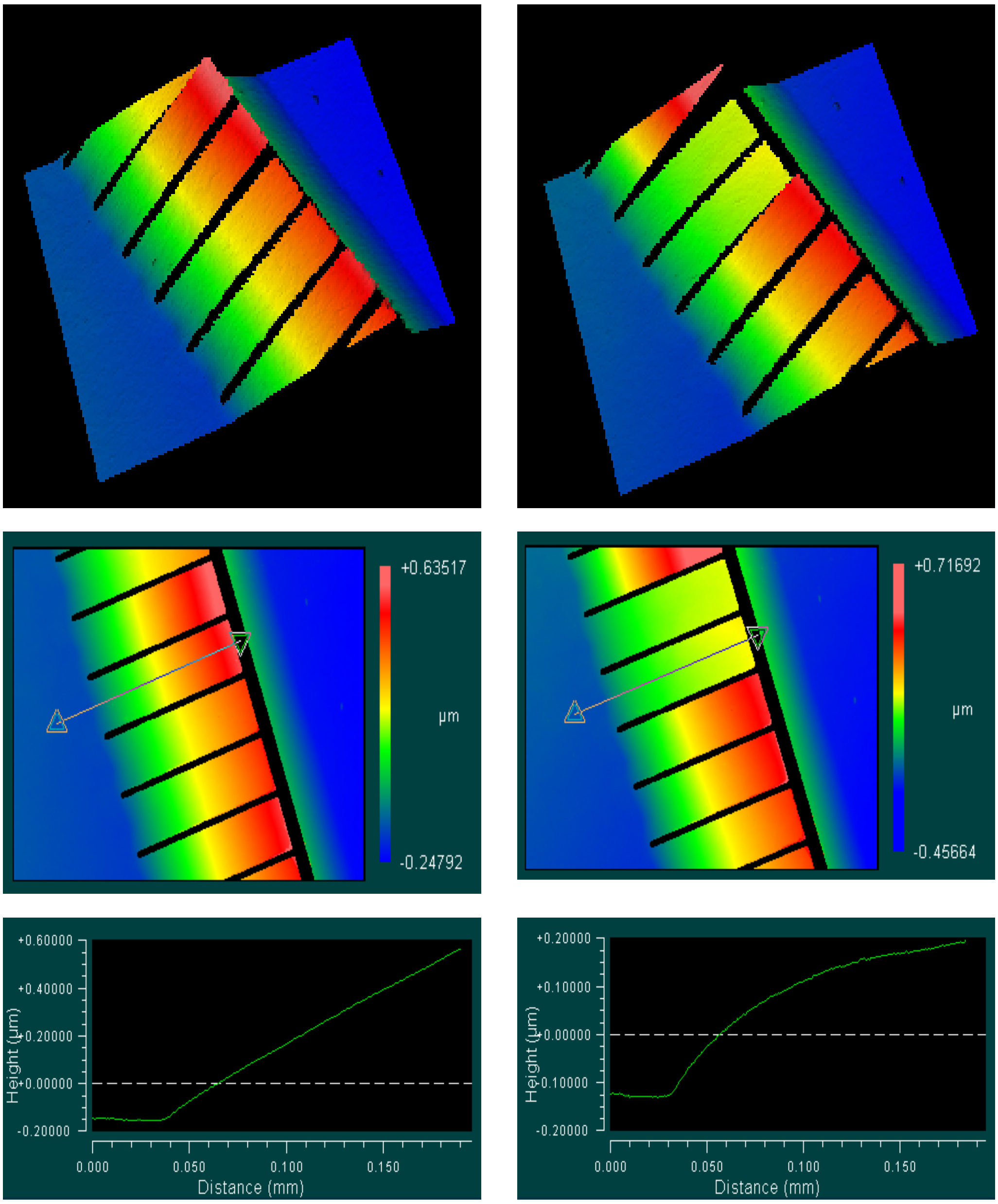

Figure 5.10: Fundamental resonant mode phase-dependent mode shapes with 180^0 out-of-phase

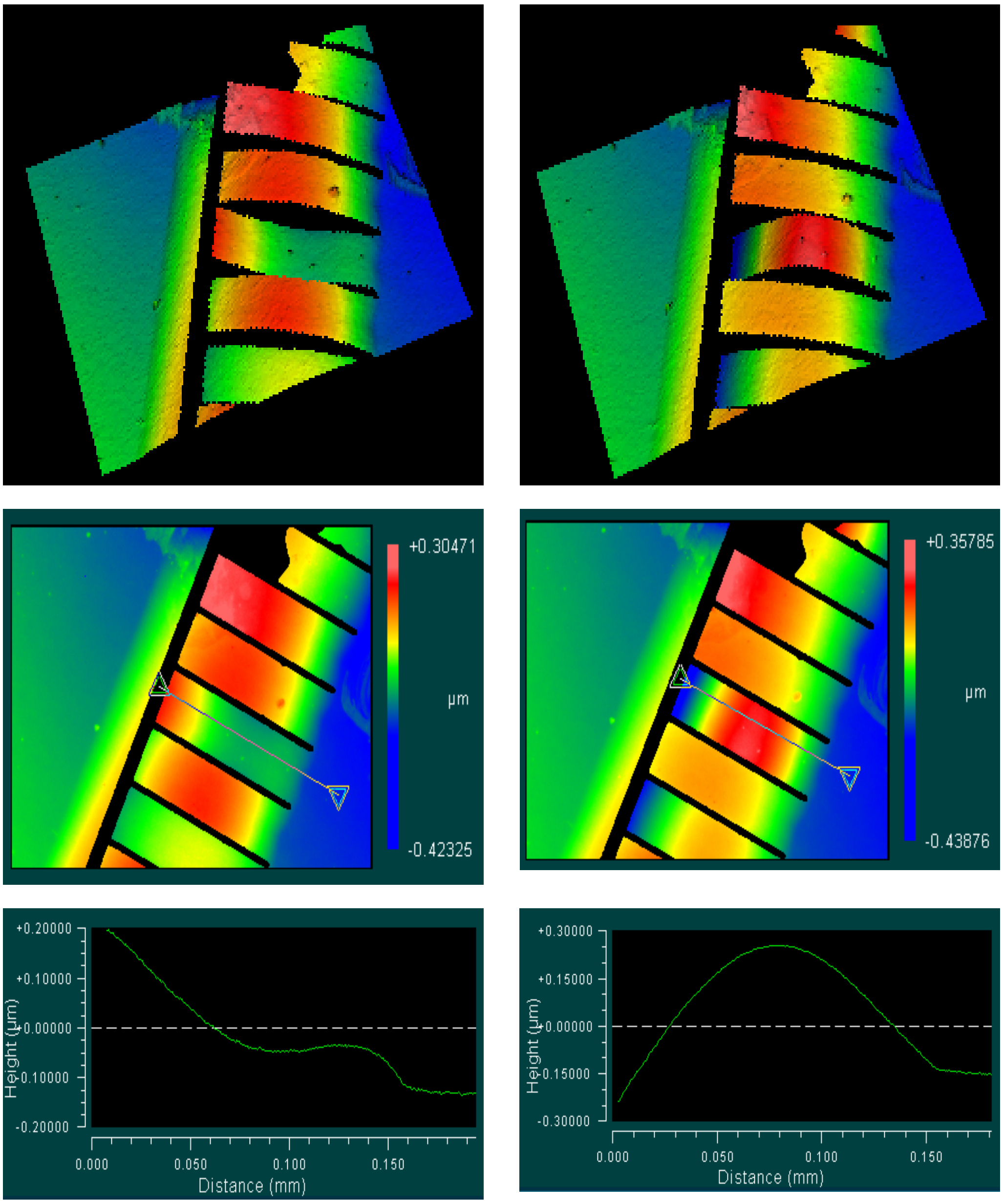

Figure 5.11: Second resonant mode phase-dependent mode shapes with 180^0 out-of-phase

5.4 A MEMS Accelerometer Design

A torsional MEMS accelerometer design for linear acceleration sensing is proposed as schematically shown in Figure (5.12). A corrugated and thin metallized proof mass is hinged by rectangular flexures to transform linear acceleration to angular displacement. Angular displacement is sensed using previously explained angular displacement detection scheme.

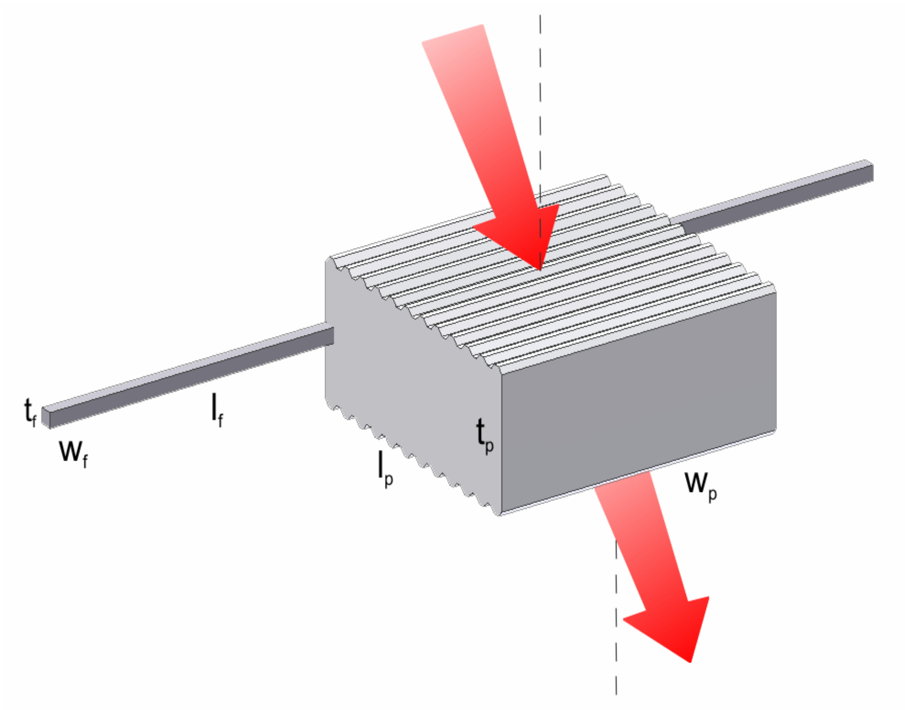

Figure 5.12: Schematic illustration of the MEMS accelerometer.

Equation of motion of the device can be formulated as

$$I\ddot{\theta} + C\dot{\theta} + \kappa\theta = \tau \tag{5.27}$$

where I is the mass moment of inertia, C is the torsional damping coefficient, κ is the torsional spring constant and τ is the applied torque. For the specified geometry, the mass moment of inertia is found as

$$I = \rho l_p t_p w_p \left(\frac{w_p^2}{3} + \frac{t_p^2}{12}\right) \tag{5.28}$$

where ρ is the mass density, l_p is the length, t_p is the thickness and w_p is the width of the proof mass. The torsional spring constant of the flexure with rectangular cross-section is given by [31]

$$\kappa = 2\frac{GJ}{l_f},$$
$$J = \frac{1}{16}K_{wt}w_f t_f^3, \tag{5.29}$$
$$K_{wt} = 5.33 - 3.36\frac{t_f}{w_f}\left(1 - \frac{t_f^4}{12w_f^4}\right)$$

where G is the torsional modulus, J is the polar moment of inertia, l_f is the length, w_f is the width and t_f is the thickness of the flexure. Mechanical properties of a device with the selected geometric and structural parameters are given in Table 5.3.

Table 5.3: Mechanical properties of the MEMS accelerometer with the selected geometric and structural parameters

Device Properties	Values	Units
Width of the flexure, $\mathbf{w_f}$	20	μm
Thickness of the flexure, $\mathbf{t_f}$	20	μm
Length of the flexure, $\mathbf{l_f}$	1000	μm
Width of the proof mass, $\mathbf{w_p}$	1000	μm
Thickness of the proof mass, $\mathbf{t_p}$	500	μm
Length of the proof mass, $\mathbf{l_p}$	1000	μm
Structural Material	Silicon	
Torsional Modulus, **G**	51	GPa
Density, **ρ**	2330	kg/m^3
Fundamental Resonance Freq., $\mathbf{f_0}$	375	Hz
Torsional spring constant, **κ**	$2.295\ 10^{-6}$	N.m
Mass moment of inertia, **I**	$4.126\ 10^{-13}$	$kg.m^2$

The angular acceleration can be expressed in terms of the linear acceleration as

$$\alpha = \frac{\tau}{I} = \frac{6w_p}{4w_p^2 + t_p^2}a \tag{5.30}$$

Substituting Eq. 5.30 into Eq. 5.27, the linear acceleration-to-angular displacement transfer function becomes

$$H(s)=\frac{\theta(s)}{a(s)}=\frac{6w_p}{4w_p^2+t_p^2}\frac{1}{s^2+\frac{C}{I}s+\frac{\kappa}{I}} \tag{5.31}$$

In terms of the natural angular frequency, ω_0 and the quality factor , Q, the transfer function in the frequency domain is expressed as

$$H(j\omega)=\frac{6w_p}{4w_p^2+t_p^2}\frac{1}{\omega_0{}^2-\omega^2+j\frac{\omega\omega_0}{Q}} \tag{5.32}$$

Similar to the derivation of the thermal-mechanical displacement noise, the thermal-mechanical acceleration noise is found as

$$\sqrt{\left\langle a_{th}^2\right\rangle_B}=\frac{4w_p^2+t_p^2}{6w_p}\sqrt{\frac{4k_BT\omega_0B}{IQ}} \tag{5.33}$$

The shot noise equivalent acceleration can be expressed in terms of the shot noise equivalent angular displacement as

$$\sqrt{\left\langle a_{sh}^2\right\rangle_B}=\frac{\kappa}{I}\frac{1}{\left(\frac{6w_p}{4w_p^2+t_p^2}\right)}\sqrt{\left\langle \theta_{sh}^2\right\rangle_B} \tag{5.34}$$

Hence, the minimum detectable acceleration is given by

$$\sqrt{\left\langle a_{tot}^2\right\rangle_B}=\sqrt{\left\langle a_{th}^2\right\rangle_B+\left\langle a_{sh}^2\right\rangle_B} \tag{5.35}$$

Noise equivalent accelerations as a function of the spectral width and beam divergence of the light source is calculated as shown in Fig.5.13. Using a monochromatic and collimated light source with 1mW optical power, for a quality factor Q of 10000 and at the temperature T of 300 K, thermal-mechanical noise limited acceleration sensing is found to be achievable which is about ten nano-g/$\sqrt{Hz}$. This is comparable with the previously reported minimum detectable accelerations of interferometric accelerometers ranging from hundreds of pico-g to tens of μ-g/$\sqrt{Hz}$. [32,33]

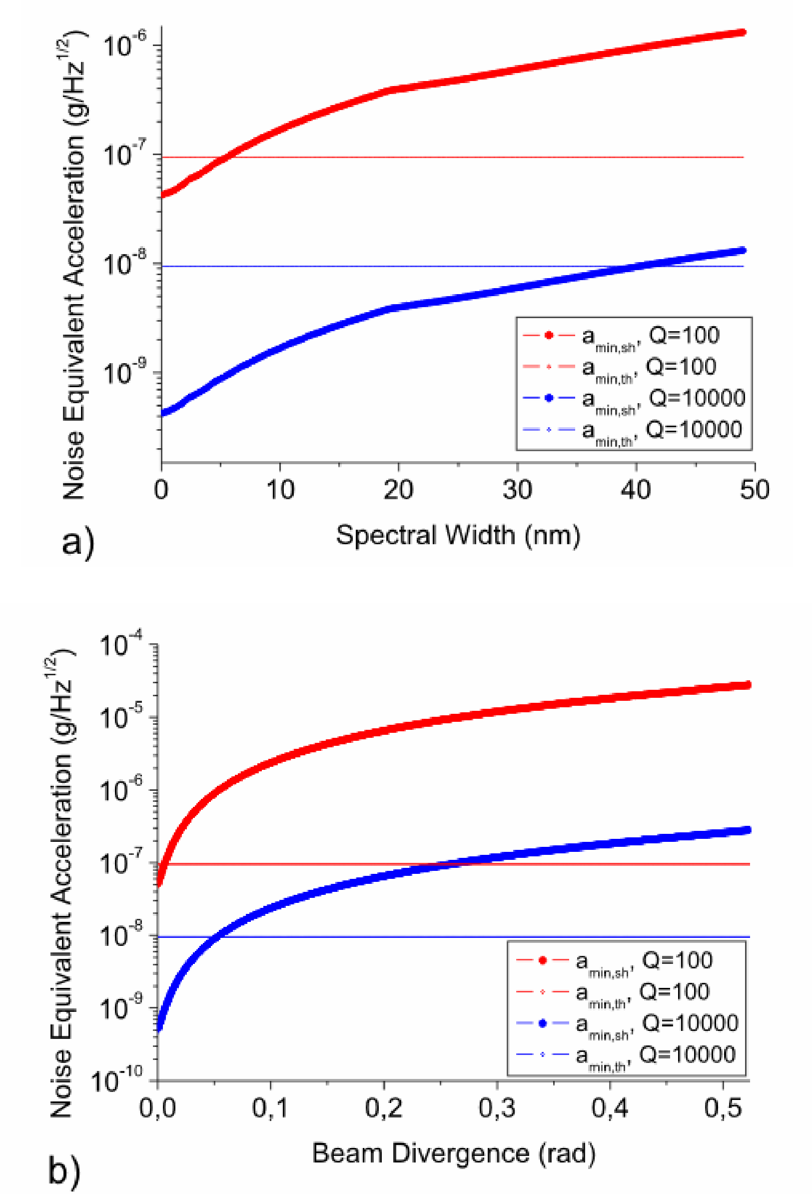

Figure 5.13: Noise equivalent accelerations as a function of the spectral width (a) and the beam divergence (b) of the light source. Optical power of the light source is taken as 1mW.

Chapter 6

Conclusions

In this study, we developed a plasmon resonance based deflection readout scheme for single and array type MEMS devices and a series of processes for fabrication of MEMS structures with plasmonic readout. We proposed a MEMS accelerometer design with nano-g noise floor.

As a first attempt, optimal parameters of a silver coated grating coupler in air media for an excitation wavelength of λ_e=633 nm and grating period of Λ=740 nm are numerically obtained using rigorous coupled wave analysis. According to our simulation results, sinusoidal and even quasi-sinusoidal (which usually outcomes as a consequence of the fabrication processes) profiles are found to yield sharper resonance curves than lamellar profile. In our particular case, former profiles result about a factor of 2 sharper resonances than the latter profile. Groove depth of 45 nm and duty cycle of 50% is found to minimize peak reflections. For reflected intensity measurements, thickness of the silver coating is suggested to be greater than 100 nm to avoid broadening of the resonance due to partial transmission. Optimal thickness for the resonant transmission case is seen to be 45 nm and discussed elsewhere.[27] Sharper resonance curves are observed at silver coating rather than gold or aluminum coatings.

Gratings with different geometric and structural properties are fabricated using several lithographic techniques. Nanoimprint lithography is used for the fabrication of quasi-sinusoidal polymeric and SiNx gratings with the period of Λ=740 nm. Master molds are prepared from commercial optical discs by applying some chemical and physical procedures.[26] In addition to well-known imprinting procedures, surface profile of polymeric gratings are transferred to SiNx sublayer by fluorine based reactive ion etching. Dry and wet etch recipes including dilute HF, dilute isopropanol and RIE are characterized for the further modification of the groove depths. Optical and electron beam lithography are used for the fabrication of lamellar SiNx gratings. Lift-off process is used rather than etch-mask process in electron beam lithography in order to produce smooth and vertical side walls. E-beam lithography is one step ahead with the achievable minimal feature sizes and custom mask definition utility, however, suffers from cost inefficiency for wide area exposures. Optical lithography is employed while patterning micron period gratings in larger scales which are rather adequate for IR wavelength plasmon excitation. Among these lithographic techniques, nanoimprint lithography with pattern transfer to sublayer procedure is the most appropriate for our demands as featuring submicron periodicity for the visible wavelength excitation, quasi-sinusoidal profile for efficient coupling, durable structural material for the subsequent microfabrication steps and large-scale and easy implementation for arrayed sensor applications.

Topographic and plasmonic properties of metallized gratings are characterized using atomic force microscopy and variable angle spectroscopic ellipsometry. RCWA simulations based on real topographic data are compared with the p-polarized reflected intensity measurements and found to be in good agreement. θ_{FWHM}'s below 1 deg is achieved as estimated by the numerical analysis.

Performance of the detection scheme is analyzed under different illumination conditions. Nanoradian per root hertz shot noise equivalent angular displacement is found to be achievable for a perfectly monochromatic and collimated light source with 1mW optical power. To give an idea, the angular displacement sensitivity falls down by 2 orders of magnitude as the spectral width is increased from 5 nm to 80 nm and 3 orders of magnitude as the beam divergence angle is expanded from 3 mrad to 300 mrad.

MEMS devices particularly designed for grating coupling are fabricated and characterized. Corrugated microcantilever and microbridge arrays are fabricated using conventional micromachining processes consisting of optical lithography, SiNx film deposition, isotropic and plane-selectively wet etching. Dynamic mechanical properties of MEMS devices are characterized by spectral and modal analysis tools. Optical beam deflection setup of an atomic force microscopy is used to gather frequency domain response and optical profilometer based on scanning white light interferometry is used to image phase-dependent mode shapes. Analytical, numerical and experimental results for resonance frequencies and flexural mode shapes are found to be consistent.

A MEMS accelerometer with plasmon resonance based readout is designed. Thermal-mechanical noise limited acceleration sensing is shown to be attainable which is about ten nano-G per root hertz for a monochromatic and collimated light source with 1 mW optical power, a quality factor Q of 10000 and the temperature T of 300 K.

Appendix A

Experimental Configuration For Displacement Detection

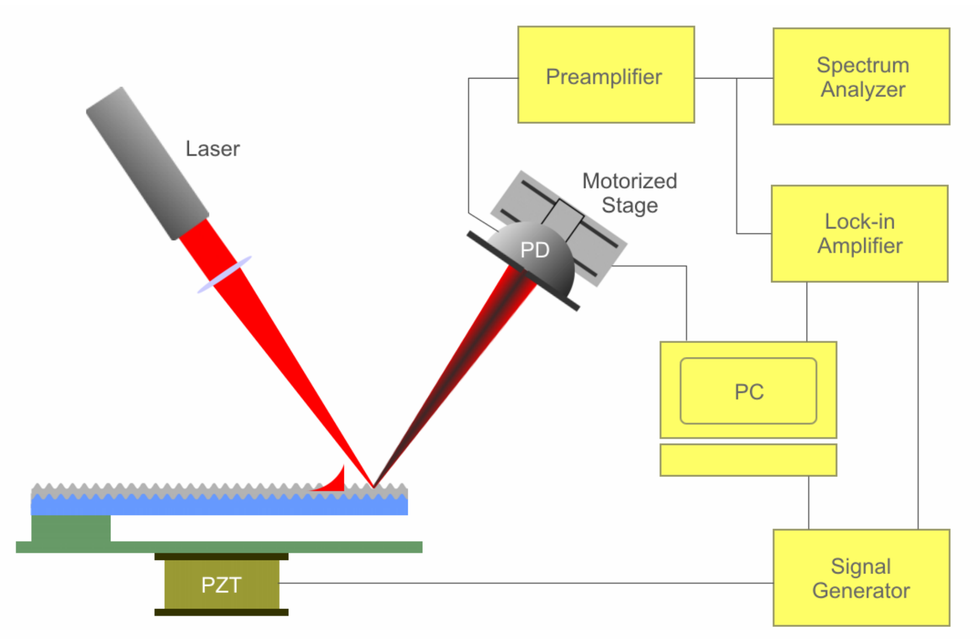

Figure A.1: Schematic illustration of the experimental configuration for SPR based micromechanical displacement detection

Experimental configuration for SPR based micromechanical displacement detection is schematically illustrated in Fig. A.1. P-polarized excitation laser beam is focused on the free end of the corrugated microcantilever at the plasmon resonance angle. Reflected beam is detected by a photodetector placed behind a narrow slit. Reflectivity spectra with respect to the angle of incidence centered around the plasmon resonance angle is obtained by scanning the reflected beam profile using a one-axis motorized translational stage. Photodetector position that maximizes the signal-to-noise ratio is selected as the bias-point of the measurement. Corrugated microcantilever is actuated by a piezo electric transducer (PZT) feed by the signal generator. Drive frequency of the device is scanned around the fundamental resonance frequency. Amplified and filtered photodetector signal by a preamplifier is both read by a spectrum analyzer and a lock-in amplifier. Spectrum analyzer generates FFT spectrum of the input signal over a wide bandwidth almost simultaneously whereas lock-in amplifier gives both amplitude and phase data within a selected bandwidth centered around the reference frequency synchronized with the signal generator. Control and synchronization of the instruments are done by a computer through the GPIB interface.

Bibliography

[1] K. L. Ekinci, Small **1**, 786 (2005)

[2] A. J. den Boef, Appl. Phys. Lett. **55**, 439 (1989)

[3] D. Rugar, H. J. Mamin, R. Erlandsson, J. E. Stern, and B. D. Terris, Rev. Sci. Instrum. **59**, 2337 (1988)

[4] D. Rugar, H. J. Mamin, and P. Guethner, Appl. Phys. Lett. **55**, 2588 (1989)

[5] D. W. Carr, L. Sekaric, H. G. Craighead, J. Vac. Sci. Tech. B **16**, 3821 (1998)

[6] C. Schönenberger and S.F. Alvarado, Rev. Sci. Instrum. **60**, 3131 (1989)

[7] G. G. Yaralioglu, A. Atalar, S. R. Manalis, and C. F. Quate, J. Appl. Phys. **83**, 7405 (1998)

[8] G. Meyer and N. M. Amer, Appl. Phys. Lett. **53**, 2400 (1988)

[9] S Alexander, L. Hellemans, 0. Marti, J. Schneir, V. Elings, P. K. Hansma, M. Longmire, and J. Gurley, J. Appl. Phys. **65**, 164 (1988)

[10] M. Tortonese, R. C. Barrett, and C. F. Quate, Appl. Phys. Lett. **62**, 834 (1993)

[11] W. C. Tang, T. C. H. Nguyen, M. W. Judy, and R. T. Howe, Sens. Actuators A **21**, 328 (1990)

[12] R. E. Mihailovich and J. M. Parpia, Phys. Rev. Lett. **68**, 3052 (1994)

[13] Putman CAJ, Grooth BGD, Hulst NFV, Greve J., J Appl Phys **72** (1):6–12 (1992)

[14] J. Homola, *Surface Plasmon Resonance Based Sensors* (Springer-Verlag, Berlin-Heidelberg-New York, 2006)

[15] J. D. Jackson, *Classical Electrodynamics* (Wiley, New York, 1998)

[16] N. W. Ashcroft and N. D. Mermin, *Solid State Physics* (International Thomson Publishing, 1976)

[17] A. Otto, Zeitschrift für Physik, **216** (4): 398-410 (1968)

[18] E. Kretschmann and H. Raether, Zeitschrift für Naturforschung, **23**A: 2135-2136 (1968)

[19] R. W. Wood, Proceedings of the Physical Society of London, **18**: 269-275 (1902)

[20] C: R. Pollock, *Fundamentals of Optoelectronics* (Richard D. Irwin, 1995)

[21] J. Lu, C. Petre, E. Yablonovitch, and J. Conway, J. Opt. Soc. Am. B **24**, 2268-2272 (2007)

[22] C. Peng and W. A. Challener, Opt. Express **12**, 6481–6490 (2004)

[23] G. Leveque and O. J. F. Martin, Proc. SPIE 5927, 592713 (2005)

[24] M. G. Moharam, E. B. Grann, and D. A. Pommet, J. Opt. Soc. Am. A **12**, 1068-1076 (1995)

[25] E. D. Palik, *Handbook of Optical Constants of Solids* (Academic, New York, 1985)

[26] B. Kaplan, H. Guner, O. Senlik, K. Gurel, M.Bayindir and A. Dana, Plasmonics, 1557-1955 (2009)

[27] K.Gurel, B. Kaplan, H. Guner, Mehmet Bayindir and A. Dana, Applied Physics Letters **94**, 233102 (2009).

[28] A. Cleland, *Foundations of Nanomechanics* (Springer-Verlag, Berlin-Heidelberg-New York, 2003)

[29] D.M. Karabacak, Ph.D. Dissertation, Boston University (2008)

[30] H. Seidel *et al.*, Journal of Electrochemical Society, **137** (11): 3612–3632 (1990)

[31] H. Urey, Proc. SPIE Optical Scanning II 4773, pp. 27–37 (2002)

[32] M. Stephens, Rev. Sci. Instrum. **64**, 2612 (1993)

[33] E. B. Cooper, E. R. Post, S. Griffith, J. Levitan, S. R. Manalis, M. A. Schmidt, and C. F. Quate, Appl. Phys. Lett. **76**, 3316 (2000)